FUNCTIONAL NANOPARTICLES:

SYNTHESIS AND SIMULATION

A Thesis
Presented to
The Academic Faculty

by

Congshan Wan

In Partial Fulfillment
of the Requirements for the Degree
Master of Science in the
School of Materials Science and Engineering

Georgia Institute of Technology
December 2014

FUNCTIONAL NANOPARTICLES:

SYNTHESIS AND SIMULATION

Approved by:

Dr. Zhiqun Lin, Advisor
School of Materials Science and Engineering
Georgia Institute of Technology

Dr. Vladimir Tsukruk
School of Materials Science and Engineering
Georgia Institute of Technology

Dr. Valeria Milam
School of Materials Science and Engineering
Georgia Institute of Technology

Date Approved: Nov 12, 2014

To my parents

ACKNOWLEDGEMENTS

I would like to thank many people without whose support this thesis would never been finished. First of all, I would like to thank my advisor, Prof. Zhiqun Lin, for his innovative insights on the projects. His trust, encouragement and generosity were also indispensible to the completion of this project. I would also like to thank the committee members, Prof Vladimir Tsukruk and Prof. Valeria Milam, for their questions and comments.

I was blessed to work with a group of outstanding colleagues. Dr. Xinchang Pang must be especially thanked for all the knowledge and techniques he shared with me, from the mechanism of atomic transfer radical polymerization (ATRP) to the operation principle of gel permeation chromatography (GPC). What's more, his idea of using β-cyclodextrin as micro-initiator was the foundation on which part of my projects was based. I would like to thank Chaowei Feng, a Ph.D. candidate in the group, for all the helpful discussion and guidance. In the early stage of the project, it was him who taught me necessary apparatus operations and led me into the chemistry world. He also took the lead in the silica nanoparticle project we worked on together. I would like to thank all the senior group members, postdoctoral fellow Dr. Ming He, Ph.D. candidate Bo Li, Jaehan Jung, Beibei Jiang, James Iocozzia, and Yanjie He for their kindly help on many occasions, such as operating TEM, XRD and Raman, etc. Also, I would like to thank the students who joined the group with me at the same time for the active discussion and joint learning. The staff at the School of Materials Science and Engineering also deserve special thanks for their help in assisting my stay at Georgia Tech.

Finally, I would like to thank my parents. They always encourage me, clear my confusions, guide me through the puzzles, and support me no matter what decision I make. No word can express my gratitude I feel towards my parents for giving me so many opportunities in life.

Congshan Wan

Gerogia Institute of Technology

November 2014

TABLE OF CONTENTS

LIST OF TABLES

LIST OF FIGURES

SUMMARY

Functional nanoparticles have garnered considerable attention due to their intriguing physical properties at the nanoscale for a broad range of applications, such as photocatalysis, capacitive energy storage, thermoelectric power generation, solar energy harvesting, flexible and transparent electronics, drug delivery, biomolecular electronics, and analytic chemistry, etc. Successful synthesis of nanoparticles and precise control over their shapes are critical to achieving desired functions. In the first part of my thesis, an effective synthetic route to plain nanoparticles is briefly introduced. Based on this general route, the synthesis of solid iron oxide nanoparticles and a slightly modified synthetic method of solid silica nanoparticles are presented in detail. In the second part of my thesis, simulation of optical absorption spectra and plasmonic near-field maps of gold nanoparticle and gold/titanium oxide nanoparticle are explored, and the effectiveness of simulation in predicting, optimizing, and guiding experimental design is emphasized.

CHAPTER 1

INTRODUCTION

Nanoparticles exhibit many unusual properties compared with bulk materials due to the special interface specifically observed on the scale of 1-100 nm. New properties resulted from the size effect render nanoparticles a promising candidate for many applications. For example, some noble metal nanoparticles, such as gold and silver, generate surface plasmon resonance upon illumination, which gives rise to the enhancement in optical absorption. In another example, semiconductor nanoparticles, such as CdSe, demonstrate the quantum confinement effect, and their emission spectra are dictated by nanoparticle size [1]. Since material properties are greatly dependent on size and shape in the nanometer scale, a robust synthetic method that could control these factors is highly desirable. The large surface area to volume ratio of nanoparticles provides more active sites for chemical and physical interactions; on the other hand, attractive interaction such as van der Waals force, usually results in undesired agglomeration of nanoparticles which significantly affect microstructural homogeneity. Therefore, surface modification, such as adding ligands, is important to achieve monodispersed nanoparticle collections.

In this thesis, a two-step nanoparticle synthetic method is introduced: the first step is the utilization of β-cyclodextrin as a nanoreactor to synthesize star-like block copolymer templates via atom-transfer radical polymerization (ATRP), and the second step is the introduction of precursors with desired elements into above-mentioned templates to form inorganic nanoparticles. A schematic diagram of the synthetic route is shown in Figure 1. This synthetic route enables precise shape control of nanoparticles by tuning polymer chain length, and various morphologies, such as plain, hollow, core-shell, and multi-shell structures, can be made by polymerizing different types of monomers.

This two-step nanoparticle synthetic method can be simplified if the desired elements are carried on the polymer side chains. In this case, the second step, which is adding precursors, is no longer necessary.

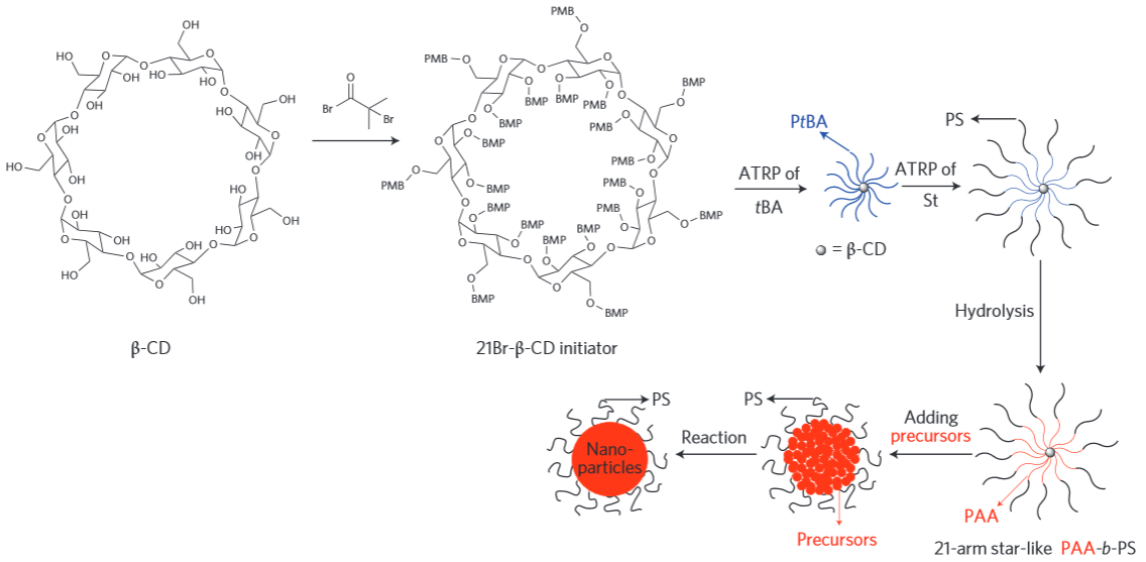

Figure 1: Schematic diagram showing the polymer template method of nanoparticle fabrication, reproduced from [2].

1.1 Background

1.1.1 Atom Transfer Radical Polymerization

Atom transfer radical polymerization (ATRP) is a type of controlled/living radical polymerization (CRP) mediated by a transition metal complex (M_t^n-Y/ligand, where M_t represents a transition metal, n represents the oxidation state of the metal, and Y represents a halogen atom or other ligand). The general mechanism for ATRP is shown in Figure 2 [3]. Equilibrium is established between an activation process and a deactivation process with rate constant indicated by k_{act} and k_{deact}, respectively. A radical R• (active species) is quickly generated when a halogen atom X transfers from the dormant species

R-X to the transition metal complex. This free radical can then react with a monomer M containing a carbon double bond so that the polymer chain propagates at the rate of k_p. Since k_{deact} is larger than k_{act}, the dormant state is preferred in the equilibrium, which reduces the polymerization rate k_p. In a well-controlled ATRP, termination of polymer chains (with the rate constant k_t) rarely occurs until ~100% conversion [4]. Fast initiation, preferred deactivation, slow propagation and small termination rate result in uniform chain length and low polydispersity.

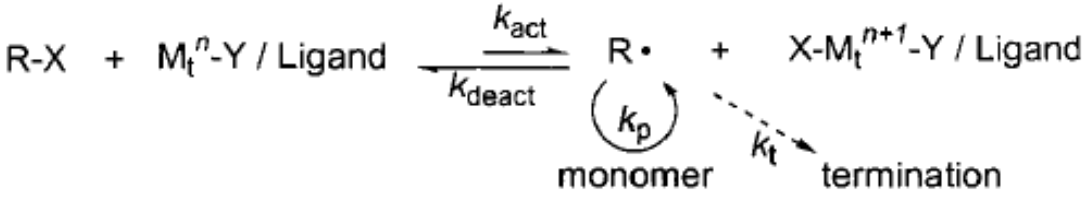

Figure 2: Reaction scheme of ATRP, reproduced from [3].

1.1.2 Components of Atom Transfer Radical Polymerization

- Catalyst

As the most important component in ATRP, catalysts are crucial to realize efficient atom transfer reversibility and to prevent nonlinear growth of molecular weight. In order to design efficient transition metal catalysts, several requirements must be considered. First, two oxidation states with one electron charge difference must be presented in the transition metal. Second, the transition metal must have a large affinity to a halogen atom. Third, the ligand that envelopes the metal center should be flexible, allowing the addition of an extra halogen atom to the metal. Lastly, the catalyst complex should mediate the equilibrium effectively for a particular system and have a good control over polymerization speed [5].

Many transition metal complexes, including the complex of molybdenum (group 6), rhenium (group 7), ruthenium and iron (group 8), rhodium (group 9), nickel and palladium (group 10), and copper (group 11) [5], have been reported in the polymerization of styrene, methyl acrylate (MA), and methyl methacrylate (MMA) . Copper catalysts, in particular, have the advantages of good versatility and low cost, and they are the focus of this thesis. Common ligands that form coordination bonds with the copper center are 2,2'-bipyridine (byp) and *N*,*N*,*N*′,*N*′,*N*″-pentamethyldiethylenetriamine (PMDETA), whose chemical structures are shown in Figure 3 (A) and (B), respectively. The incorporation of a halogen atom X (X = Br or Cl) into the copper complex consisted of byp and PMDETA is respectively shown in Figure 4 (A) and (B).

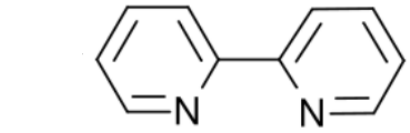

(A)

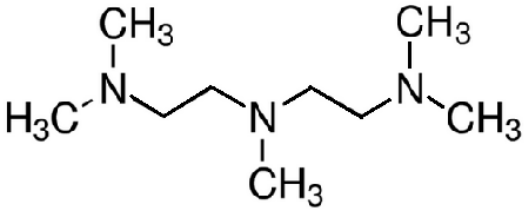

(B)

Figure 3: Chemical structure of ligand: (A) byp and (B) PMDETA.

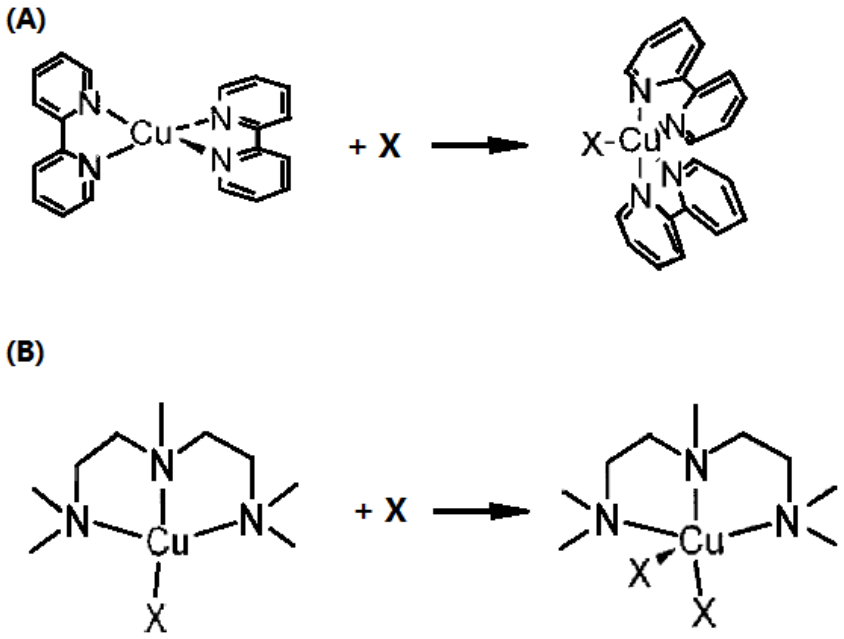

Figure 4: Incorporation of a halogen atom X into copper complex: (A) Cu(byp) and (B) CuX(PMDETA).

- Initiator

In order to produce polymers with low polydispersities, fast initiation compared with propagation and reduced side reactions are necessary. Various halogenated initiators have been applied in ATRP, such as alkyl halides, benzylic halides, α-haloesters, α-haloketones, α-halonitriles, and sulfonyl halides [5]. Shape of the resulting polymers can be controlled by the functionality of the initiators. In this thesis, initiators with multiple initiating sites are required to synthesize star-like polymers. β-cyclodextrin (β-CD), whose structure is shown in Figure 5, is chosen as the core of the initiator since its 21 hydroxyl groups (–OH) could be modified by 2-bromoisobutyryl bromide and serve as the initiating sites.

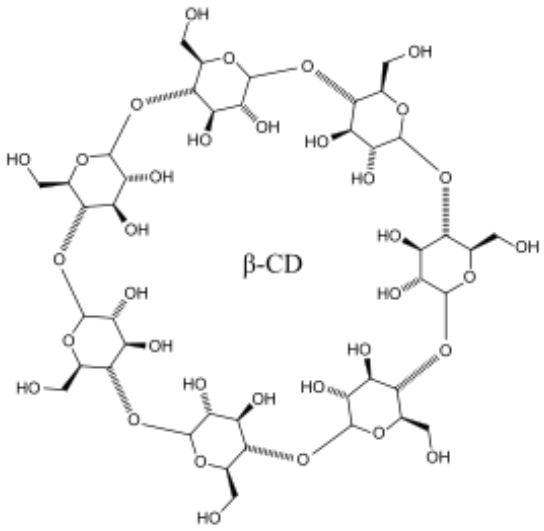

Figure 5: Structure of *β*-cyclodextrin.

The 21 hydroxyl groups on *β*-CD are directly esterified by reacting with 2-bromoisobutyryl bromide as depicted in Figure 6. This is because Br is a good leaving group, and the hydroxyl group on *β*-CD serves as the nucleophile that attacks the carbonyl carbon, resulting in nucleophilic carbonyl substitution. The final macromolecule, heptakis [2, 3, 6-tri-*O*-(2-bromo-2-methyl-propionyl) - *β*-cyclodextrin], denoted 21 Br-*β*-CD, has the structure shown in Figure 7. In the presence of copper catalysts, the Br atom is easily detached from the tertiary carbon, leaving behind a free radical, as shown in Figure 8.

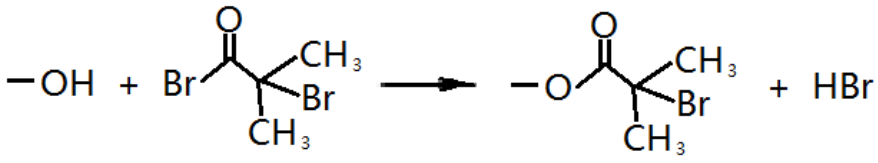

Figure 6: Esterification process of a hydroxyl group on *β*-CD.

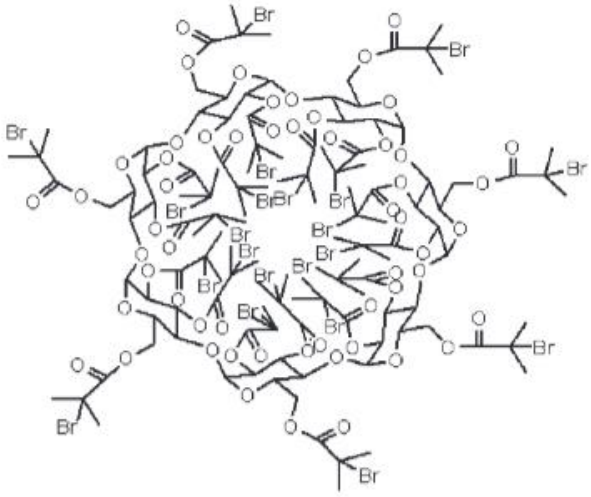

Figure 7: Structure of 21 Br-*β*-CD.

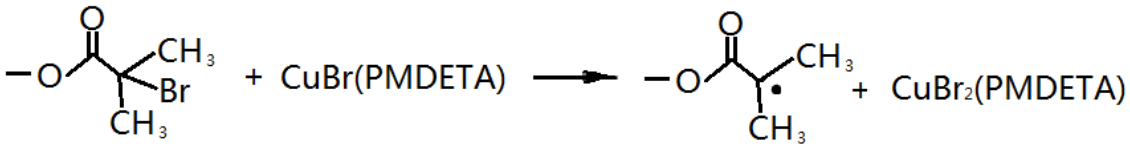

Figure 8: Radical initiation by Br atom detachment mediated by Cu catalyst complex.

♦ Monomer

Many reactive monomers, such as styrene, (meth)acrylate, (meth)acrylamide, and acrylonitrile, etc, have been polymerized using ATRP. These monomers typically possess substituent that can stabilize the propagating radicals [3]. Less reactive monomers, such as olefin, halogenated alkenes, and vinyl acetate, have not been successfully synthesized [3]. This is because polymerization rate is determined by the equilibrium constant K_{eq} ($K_{eq} = k_{act}/k_{deact}$), and atom transfers can hardly occur when equilibrium constant is too small. Moreover, a particular type of monomer usually has a unique reaction rate which is largely affected by concentration, catalyst, temperature, solvent, and other external

conditions. As a result, ATRP is a sensitive technique requiring careful controls over many parameters.

This thesis discusses the polymerization of styrene, *tert*-butyl acrylate (tBA) and 3-(trimethoxysilyl) propyl methacrylate (TMSPMA), and their chemical structures are shown in Figure 9 (A), (B), and (C), respectively.

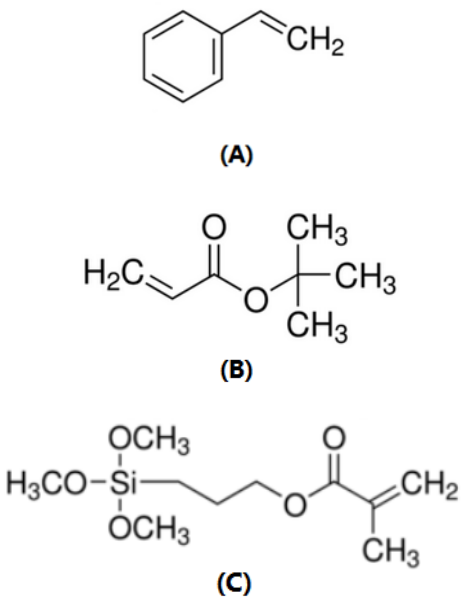

Figure 9: Chemical structure: (A) styrene, (B) tBA, and (C) TMSPMA.

1.1.3 Characterization

- Chemical Characterization
  - Nuclear Magnetic Resonance Spectroscopy

In organic chemistry, nuclear magnetic resonance (NMR) spectroscopy is used to identify the functional groups and molecule structures based on nuclear magnetic resonances. In the presence of external magnetic field, a spin $\frac{1}{2}$ nucleus generate two spin states, one in the direction of the external field and the other in the opposite direction,

separated by an energy difference ΔE which is defined by the type of nuclei (element and surroundings). Nuclei can be excited by radio frequency pulses from the lower energy state to the higher energy state. The energy absorbed, ΔE, characterizes the resonance frequency. NMR signal is affected by reference frequency and the strength of applied magnetic field. In order to remove the influence of these factors, chemical shift, in unit of parts per million (ppm), is defined to be a resonance locator. An Atom with an odd number of neutrons and/or an odd number of protons is NMR active. ^{1}H active and ^{13}C active NMR spectroscopy are commonly used. Repeated acquisition must be taken so that the signal to noise ratio is minimized.

- Polymer Characterization
  - Gel Permeation Chromatography

Gel Permeation Chromatography (GPC) is a characterization technique that measures the molecular weight distribution of a batch of polymers. Its instrument consists of a column filled with porous particles or gels, a pump and a detector. A good solvent for the polymers under test is a necessary carrier for analyte delivery. What GPC truly measures is the molecular volume and the corresponding viscosity. Polymers with smaller molecular weights, which have relatively smaller molecular volumes, tend to be trapped in the pores of gels for a longer time, thus reaching the detector later. This can be reflected from the GPC chromatogram (signal versus time) where the peaks corresponding to larger molecular weights appear earlier while the peaks corresponding to smaller molecular weights appear later. GPC provides the results of the number average molecular weight (M_n), the weight average molecular weight (M_w), the size average molecular weight (M_z), or the viscosity molecular weight (M_v).The molecular weight distribution can be indicated by polydispersity index (PDI), which is defined as

the ratio of M_w and M_n ($PDI = \frac{M_w}{M_n}$). PDI has the value equal to or larger than one. PDI equal to one indicates a uniform polymer chain length.

- Nanoparticle Characterization

  - Transmission Electron Microscopy

Transmission electron microscope (TEM) resolves small features down to the angstrom (10^{-10}m) size based on the interaction between the electron beam and the specimen. The high resolution is resulted from the small de Broglie wavelength of electrons. Electrons are generated by an electron gun and focused onto a thin specimen slice by magnetic lenses. Electrons are scattered by atoms in the specimen and the deflections are determined by the crystal structure. TEM provides both specimen images in the real space and diffraction patterns in the reciprocal space.

  - Atomic Force microscopy

Atomic force microscope (AFM) enables three-dimensional measurements of the specimen, which is a superior advantage that other electron microscopes don't possess. AFM demonstrates resolution in angstrom scale and usually a better resolution in vertical direction (z direction) than in horizontal plane (x-y plane). AFM utilizes a cantilever with a sharp tip to scan the specimen surface. A force is developed when the tip is in close proximity to the surface, resulting in the deflection of the cantilever. By measuring the deflection using a piezoelectric detector, the surface morphology of the specimen can be determined. Three modes of operation exist in AFM: contact mode, non-contact mode, and tapping mode. In contact mode, deflection of the cantilever is kept constant (constant height or constant force); in non-contact mode, the cantilever tip is oscillated at the resonance frequency and the amplitude of the oscillation is kept constant; in tapping

mode, the tip intermittently contacts the surface, and this mode gives better resolution with little sample damage.

1.1.4 Simulation of Optical Properties

- Localized Surface Plasmon Resonance

The optical properties of nanomaterials have been extensively investigated due to their potential application in molecular-specific imaging, chemical and biological sensing, and nano-optical devices [7]. Noble metal nanoparticles, in particular, are superior light absorbers and scatterers due to their strongly enhanced plasmon resonance located in the visible range [8]. The origin of the localized surface plasmon resonance may be explained as follows. When the size of the nanoparticles are comparable to or smaller than the mean free path of the free electrons in the noble metals, all the interactions with electromagnetic waves take place at the nanoparticle surface. When the wavelengths of the incoming electromagnetic waves are much larger than the nanoparticle sizes, the electron clouds at the nanoparticle surface will synchronize with the incoming optical wave and oscillate in resonance with the optical wave frequency. Figure 10 presents the surface charge distribution of nanoparticles at a particular time, and it is observed that the charges are polarized to oppose external electric field. The resonance condition depends on the size and shape of nanoparticles as well as the dielectric constants of materials and surroundings. Nanoparticles made of other elements also demonstrate localized plasmon, yet in other range of the spectrum, and the reason of surface plasmon resonance may be due to quantum confinement effect, such as in copper and lead nanoparticles [8].

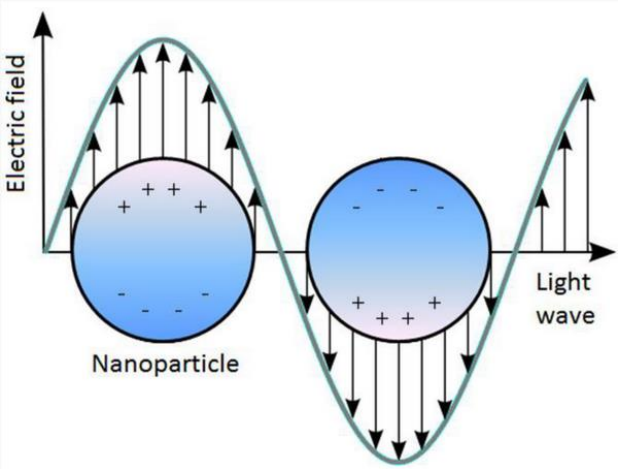

Figure 10: Localized surface plasmon resonance induced by external electric field, reproduced from [9].

♦ Theory of Electromagnetic Waves

Electromagnetic field, generated by a distribution of electric charges, is postulated by Maxwell's equations, whose differential forms are written as:

$$\nabla \times \mathbf{H} = \mathbf{J} + \frac{\partial \mathbf{D}}{\partial t} \qquad \text{eq. 1.1}$$

$$\nabla \times \mathbf{E} = -\frac{\partial \mathbf{B}}{\partial t} \qquad \text{eq. 1.2}$$

$$\nabla \cdot \mathbf{D} = \rho \qquad \text{eq. 1.3}$$

$$\nabla \cdot \mathbf{B} = 0 \qquad \text{eq. 1.4}$$

where **E** is the electric field intensity, **D** is the electric displacement (or flux) density, **H** is the magnetic field intensity, **B** is the magnetic flux intensity, and ρ is the electric charge density. The above Maxwell's equations are applicable for general time-varying fields. Equation 1.1 and Equation 1.2 are referred to as Ampere's law and Faraday's law, respectively.

By conservation of charges, the equation of continuity must be satisfied:

$$\nabla \cdot \mathbf{J} = -\frac{\partial \rho}{\partial t} \qquad \text{eq. 2}$$

There exist several constitutive relations that describe the macroscopic properties of matters:

$$\mathbf{D} = \varepsilon_0 \mathbf{E} + \mathbf{P} \quad \text{eq. 3}$$

$$\mathbf{B} = \mu_0 \mathbf{H} + \mathbf{M} \quad \text{eq. 4}$$

$$\mathbf{J} = \sigma \mathbf{E} \quad \text{eq. 5}$$

where ε_0 is the permittivity of vacuum ($\varepsilon_0 = \frac{1}{c_0^2 \mu_0} \approx \frac{1}{36\pi} \times 10^{-9} = 8.854 \times 10^{-12}$ F/m), μ_0 is the permeability of vaccum ($\mu_0 = 4\pi \times 10^{-7}$ H/m), **P** is the electric polarization vector (volume density of electric dipole moments), **M** is the magnetization vector (volume density of magnetic dipole moments), and σ is the electrical conductivity. When material property is linear (property doesn't depend on the intensity of electromagnetic field), the following relations hold:

$$\mathbf{P} = \varepsilon_0 \chi_e \mathbf{E} \quad \text{eq. 6}$$

$$\mathbf{M} = \mu_0 \chi_m \mathbf{H} \quad \text{eq. 7}$$

$$\mathbf{D} = \varepsilon_0 (1 + \chi_e) \mathbf{E} = \varepsilon_0 \varepsilon_r \mathbf{E} = \varepsilon \mathbf{E} \quad \text{eq. 8}$$

$$\mathbf{B} = \mu_0 (1 + \chi_m) \mathbf{H} = \mu_0 \mu_r \mathbf{H} = \mu \mathbf{H} \quad \text{eq. 9}$$

where χ_e is the electric susceptibility, χ_m is the magnetic susceptibility, ε_r is the relative permittivity, $\mu_r$is the relative permeability, ε is the permittivity of the material, and μ is the permeability of material.

Electromagnetic waves scatter when encountering obstacles, e.g. nanoparticles. A part of the scattering comes from the change of propagation direction from original wave direction, and this takes place when the incoming wave interacts with the oscillating free electrons in the nanoparticles. Another part of the scattering comes from the secondary radiation of nanoparticles resulted from the accelerated electrons in the incident electromagnetic field. The accelerated electrons may also absorb a portion of the incident energy in the form of thermal energy (Joule heating). The sum of scattering and absorption is called extinction which represents the total energy loss of incident waves upon interacting with nanoparticles [10]. In order to quantify the energy power that is lost

either by scattering or absorption, a physical quantity, called cross-section, is defined as a hypothetical area that describes the probability of light being scattered or absorbed.

The scattering of electromagnetic waves by spherical nanoparticles is described by Mie Theory. The mathematical deviation of Mie Theory is complex and only part of the theory is introduced. The following discussion is under the assumption of plane wave incidence. When the incident wave is scattered, the total field consists of two parts, incident part and scattered part. The total electric field and total magnetic field are represented by Equation 10 and Equation 11, respectively:

$$\mathbf{E}_{\mathrm{tot}} = \mathbf{E}_{\mathrm{inc}} + \mathbf{E}_{\mathrm{sca}} \qquad \text{eq. 10}$$

$$\mathbf{H}_{\mathrm{tot}} = \mathbf{H}_{\mathrm{inc}} + \mathbf{H}_{\mathrm{sca}} \qquad \text{eq. 11}$$

Mie theory solves the scattered electric field from the following Helmholtz equation:

$$\boldsymbol{\nabla} \times \left(\frac{1}{\mu_{\mathrm{r}}} \boldsymbol{\nabla} \times \mathbf{E}_{\mathrm{sca}}\right) - {k_0}^2 \left(\frac{\varepsilon_{\mathrm{r}}}{\mu_0} - i\frac{\sigma}{\omega\varepsilon_0\mu_0}\right)\mathbf{E}_{\mathrm{sca}} = 0 \qquad \text{eq. 12}$$

where ω is the optical wave angular frequency, and i equals $\sqrt{-1}$. Equation 12 is derived from the Maxwell's equations (Equation 1.1 and Equation 1.2). The deviations are shown as follows, assuming non-magnetic and isotropic media (Equation 8 and Equation 9 satisfied):

$$\nabla \times \mathbf{H} = \mathbf{J} + i\omega\mathbf{D} = \sigma\mathbf{E} + i\omega\varepsilon\mathbf{E} \qquad \text{eq. 13}$$

$$\nabla \times \mathbf{E} = -i\omega\mu\mathbf{H} \qquad \text{eq. 14}$$

Find curl of Equation 14 and plug in Equation 13:

$$\nabla \times \nabla \times \mathbf{E} = -i\omega\mu\nabla \times \mathbf{H} = -i\omega\mu(\sigma\mathbf{E} + i\omega\varepsilon\mathbf{E})$$

$$\nabla \times \frac{1}{\mu}\nabla \times \mathbf{E} - \omega^2\left(\varepsilon - i\frac{\sigma}{\omega}\right)\mathbf{E} = 0$$

$$\omega = \frac{k_0}{\sqrt{\varepsilon_0\mu_0}}$$

Based on the scattered electric field, the scattered magnetic field is calculated from Faraday's law:

$$\mathbf{H}_{\mathrm{sca}} = -\frac{1}{i\omega\mu}\nabla \times \mathbf{E}_{\mathrm{sca}} \qquad \text{eq. 15}$$

The scattering power (W_{sca}) is calculated by integrating the time average Poynting vector (energy flux) over an imaginary spherical surface around the nanoparticle:

$$\mathrm{W}_{\mathrm{sca}} = \oiint Re(\mathbf{E}_{\mathrm{sca}} \times \mathbf{H}^*_{\mathrm{sca}}) \cdot \mathbf{n}\mathrm{dS} \qquad \text{eq. 16}$$

where $\mathbf{S} = \mathbf{E} \times \mathbf{H}$ is the poynting vector.

The absorption power (W_{abs}) is calculated by integration of the energy loss rate over the nanoparticle volume:

$$\mathrm{W}_{\mathrm{abs}} = \oiiint Re(\mathbf{J}_{\mathrm{tot}} \cdot \mathbf{E}^*_{\mathrm{tot}} + i\omega\mathbf{B}_{\mathrm{tot}} \cdot \mathbf{H}^*_{\mathrm{tot}})\mathrm{dV} \qquad \text{eq. 17}$$

where $\mathbf{J}_{\mathrm{tot}}$ is the total electrical current density and it is the sum of electrical conduction current density and displacement current density: $\mathbf{J}_{\mathrm{tot}} = \sigma\mathbf{E} + i\omega\mathbf{D}$. The first part of the sum inside the integral represents resistive loss (Joule heating). The second part of the sum inside the integral represents the magnetic loss, which is usually too small to be considered.

The scattering cross-section (σ_{sca}) and absorption cross-section (σ_{abs}) are obtained by dividing the power by incident energy flux (P_{inc}):

$$\sigma_{\mathrm{sca}} = \frac{\mathrm{W}_{\mathrm{sca}}}{\mathrm{P}_{\mathrm{inc}}} \qquad \text{eq. 18}$$

$$\sigma_{\mathrm{sca}} = \frac{\mathrm{W}_{\mathrm{sca}}}{\mathrm{P}_{\mathrm{inc}}} \qquad \text{eq. 19}$$

where $\mathrm{P}_{\mathrm{inc}} = \frac{1}{2}Re(\mathbf{E}_{\mathrm{inc}} \times \mathbf{H}^*_{\mathrm{inc}}) = \frac{1}{2\eta}|\mathbf{E}_{\mathrm{inc}}|^2\hat{\mathbf{k}}$. Note for an incident plane wave, the magnetic field is defined as $\mathrm{H}_{\mathrm{inc}} = \frac{1}{\eta}\hat{\mathbf{k}} \times \mathbf{E}_{\mathrm{inc}}$, where $\hat{\mathbf{k}}$ is the propagation direction of the electromagnetic wave, and $\eta = \sqrt{\frac{\mu}{\varepsilon}}$.

- Simulation Softwave
  - COMSOL Multiphysics® 4.4

COMSOL encompasses a vast variety of modules, such as ACDC module, RF module, wave optics module, heat transfer module, etc, and it is a versatile tool for simulation of single physics as well as multiphysics. Calculations in COMSOL are based on finite element method. In this thesis, the module used was *Radio Frequency*, *Electromagnetic Waves, Frequency Domain* (emw).

- Finite Element Method

Finite element method (FEM) approximates the solution to the boundary value problems of partial differential equations by subdividing the whole domain into many small sub-domains. FEM assumes constant parameters for each of the sub-domains and rewrites the complicated differential equations in a matrix form, or a set of linear equations. The equation used for simulating electromagnetic problem is Equation 12.

1.2 Research Objectives

Star-like block copolymers are versatile templates for synthesizing a large variety of nanoparticles. ATRP is a robust technique to control polymer chain lengths and consequently control particle sizes. One objective of the research is to learn the basic techniques of ATRP and nanoparticle synthesis, and demonstrate their feasibility via simple practices. Another objective is to utilize simulation tools in order to characterize, prove, and predict properties of nanoparticles. In this thesis, the simulation of optical properties is demonstrated.

CHAPTER 2

SYNTHESIS

In this chapter, synthesis route of Fe_3O_4 and SiO_2 nanoparticles are introduced in detail. All routes start with the esterification of *β*-CD, followed by ATRP of polymer templates, but subsequent procedures are slightly different. The synthesis of Fe_3O_4 nanoparticle requires a two-step process: the first step is the synthesis and hydrolysis of star-like poly(*tert*-butyl acrylate)-*b*-polystyrene (PtBA-*b*-PS) template, and the second step is the reaction of metal precursors ($FeCl_2$/$FeCl_3$) with block copolymer templates. For the SiO_2 nanoparticle synthesis, the star-like polymer poly(3-(trimethoxysilyl) propyl methacrylate**)** (PTMSPMA) already contains Si elements, so no additional precursors are required. For both synthesis methods, the final procedure is the sintering, either in air or in inert gas, in order to completely remove organic parts.

2.1 Experimental Procedures

2.1.1 Preparation of Initiator

- Materials Used

β-cyclodextrin (β-CD, Sigma-Aldrich) and 2-bromoisobutyryl bromide (98%) were used directly. Other chemicals necessary in this preparation were toluene, *N*-methyl-2-pyrrolidone (NMP), hexane, chloroform, $NaHCO_3$, and $MgSO_4$.

♦ Procedures

β-CD was first desiccated by azeotropic distillation. 6.82 g of *β*-CD (white powder) was dispersed in 100 ml of toluene and then distilled under atmospheric pressure. The temperature was set at about 120° C. A schematic diagram of the distillation apparatus is shown in Figure 11.

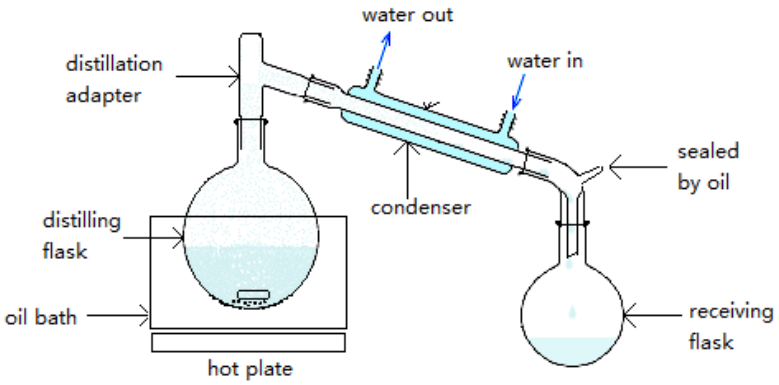

Figure 11: Schematic diagram of distillation apparatus for *β*-CD.

After liquid in distilling flask was completely removed, 60 ml of NMP was added into the round-bottom flask containing desiccated *β*-CD. *β*-CD was dissolved in NMP and the solution was stirred vigorously. The round-bottom flask was capped with a septa and seated in an ice bath. Then 58 ml of 2-bromoisobutyryl bromide was added dropwise into the flask. After the ice was melted, the mixture was kept stirred for 24 hours. A schematic diagram of the above-mentioned procedure is shown in Figure 12.

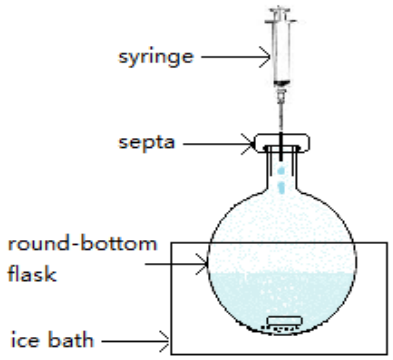

Figure 12: Schematic diagram showing the esterification procedure.

After reacting for 24 hours, a brown solution was obtained. Appropriate amount of hexane was added into the solution to precipitate the product. The mixture was stirred vigorously before settled down in the fridge. After the solids were precipitated well down to the bottom of the flask, the upper liquid was removed. Then the solids were re-dissolved in chloroform and the solution (yellow liquid) was transferred into a separation funnel. Saturated $NaHCO_3$ water solution was added into the separation funnel. The separation funnel was sealed and shook, and it was set still until the water layer and oil layer was completely separated. The oil layer was collected and the washing process was repeated until no bubbles were formed. Then deionized water was added into the oil layer and the product was washed for the last time. A schematic diagram of this procedure is shown in Figure 13. The final oil layer was transferred into an Erlenmeyer flask, $MgSO_4$ was gradually added to completely absorb water. The $MgSO_4$ hydrates were separated using a filter paper with fine holes. The final product was obtained by the reverse precipitation method. The chloroform solution containing the 21 Br-β-CD was added dropwise into cold hexane seated in ice bath. After stirred for about half an hour, the precipitation was filtered and dried in an oven.

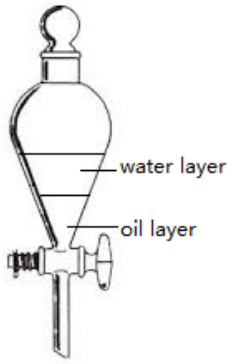

Figure 13: A separation funnel containing separated water layer and oil layer.

♦ Characterization Tool

Varian VXR-300 spectroscopy was used to acquire ^{1}H NMR spectra. $CDCl_3$ was used as solvent.

2.1.2 Preparation of Star-Like PtBA-*b*-PS Template

♦ Materials Used

▫ Synthesis of Star-like PtBA

Chemicals used in this step were 21 Br-*β*-CD, *tert*-butyl acrylate (tBA, Sigma-Aldrich, 98%), *N,N,N′,N′,N″*-pentamethyldiethylenetriamine (PMDETA, 99%), CuBr (Sigma-Aldrich, 98%), 2-butanone, acetone, and methanol.

▫ Synthesis of Star-like PtBA-*b*-PS

Chemicals used in this step were star-like PtBA synthesized in the previous step, styrene (St, Sigma-Aldrich), PMDETA, CuBr, anisole, dichloromethane and methanol.

♦ Procedures

▫ Synthesis of Star-like PtBA

tBA monomer was first distilled over CaH_2 to remove inhibitors. 0.05 g of 21 Br-*β*-CD, 0.033 g of CuBr, 0.0876 g of PMDETA, 21 ml of distilled tBA and 21 ml of 2-butanone was added into an ampule bottle. The mixture was sonicated for several minutes to fully dissolve solids and then degassed by three freeze-thaw cycles. The ampule was sealed tightly and placed in an oil bath at 60° C for 14 hours. At the end of the reaction, the ampule was put into liquid nitrogen to terminate polymerization. The product was diluted by acetone and flushed through a neutral alumina column. The mixture of methanol and deionized water in the ratio of 1:1 was added dropwise into the purified

solution until the clear solution became opaque. This precipitation process took place in ice bath. Then the mixture was settled down in the fridge for more than 8 hours and the precipitation was collected and dried in oven.

▫ Synthesis of Star-like PtBA-*b*-PS

Styrene monomer was first distilled over CaH_2 to remove inhibitors. Ampule charged with 0.5 g of PtBA, 0.035 g of CuBr, 0.085 g of PMDETA, 20 ml of distilled styrene and 20 ml of anisole was sonicated and degassed by three freeze-thaw cycles. The ampule was sealed tightly and placed in an oil bath at 90° C for 12 hours. The reaction was terminated by placing the ampule in the liquid nitrogen. The product was diluted by dichloromethane and flushed through a neutral alumina column. In cold environment, methanol was added dropwise into the purified solution to precipitate the product. The final product was dried in oven.

♦ Characterization

Gel permeation chromatography equipment Agilent110 with a G1310A pump, a G1362A refractive detector and a G1314A variable wavelength detector was used to measure the molecular weight distribution. High-performance liquid chromatography graded tetrahydrofuran (HPLC THF) was used as the eluent at 35° C at 1.0 ml/min. Its columns, one for the range of 5×10^2-2×10^4 g/mol and the other for the range of 2×10^2-3×10^6 g/mol, were calibrated with linear polystyrene.

0.002g of polymer templates was dissolved in 0.3 ml of HPLC tetrahydrofuran (THF) and filtered by a 0.45μm PTFE filter. Then the sample was injected into the GPC.

2.1.3 Hydrolysis of PtBA

- Materials Used

Chemicals used in this step were star-like PtBA-*b*-PS, trifluoroacetic acid (TFA) and dichloromethane.

- Procedures

0.3 g of PtBA-*b*-PS was dissolved in 30 ml of dichloromethane and then 10 ml of TFA was added using a glass transfer pipet. The usage of syringe should be prohibited because the strong TFA would react with the metal needle and bring unintended metal elements into the system. The resulting mixture was magnetically stirred at room temperature for 24 hours to ensure the completion of hydrolysis reaction. After PAA-*b*-PS was completely precipitated in the solvent, the product was centrifuged, washed with dichloromethane and dried in the vacuum oven at 40° C.

2.1.4 Preparation of Fe_3O_4 Nanoparticle

- Characterization Tool

JEOL 1200EX scanning/transmission electron microscope was used to characterize the size and morphology of fabricated nanoparticles.

- Materials Used

Chemicals used in this step were star-like PAA-*b*-PS, iron(II) chloride hydrate ($FeCl_2 \cdot xH_2O$), iron(III) chloride hydrate ($FeCl_3 \cdot xH_2O$), dimethylformamide (DMF), benzyl alcohol (BA), ammonium hydroxide ($NH_3 \cdot H_2O$), ethanol and toluene.

- Procedures

0.01 g of PAA-*b*-PS was dissolved in 10 ml of mixed DMF and BA in 9:1 ratio. The template was first dissolved in 9 ml of DMF and then 1 ml of BA was added into the solution. The solution was transferred into a three-neck flask. The precursors, 0.07 g of $FeCl_2 \cdot xH_2O$ (excess) and 0.094 g of $FeCl_3 \cdot xH_2O$, were added into the mixture. The apparatus was properly sealed and flushed with argon. After all solids dissolved, 1 to 2 ml of $NH_3 \cdot H_2O$ was injected into the solution via a side neck of the flask. Under argon atmosphere, the mixture reacted at 50° C for 30 min, and aged at 80° C for 2 hours. The setup is schematically shown in Figure 14. The resulting nanoparticles was collected and washed with a mixture of ethanol and toluene. The dimension of Fe_3O_4 nanoparticles was checked by TEM.

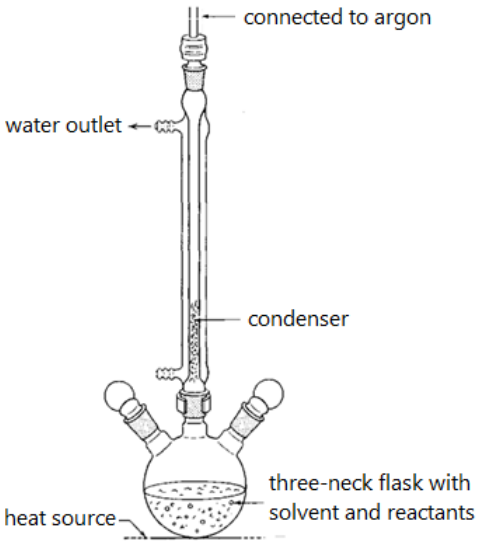

Figure 14: Reaction apparatus for obtaining Fe_3O_4 Nanoparticles.

2.1.5 Preparation of Star-Like PTMSPMA Template

- Materials Used

Chemicals used in this step were 21 Br-*β*-CD, 3-(trimethoxysilyl)propyl methacrylate (TMSPMA, Sigma-Aldrich, 98%, 1.045g/ml), *N,N,N′,N′,N″*-

pentamethyldiethylenetriamine (PMDETA, 99%), CuBr (Sigma-Aldrich, 98%), anhydrous toluene, anhydrous dichloromethane, and anhydrous petroleum ether .

- Procedures

0.0203 g of 21 Br-β-CD (star-like initiator), 0.0143 g of CuBr (catalyst), 0.0173 g of PMDETA (catalyst), 4.85 ml of TMSPMA (monomer) and 5 ml of anhydrous toluene (solvent) were added into an ampule (molar ratio of 21 Br-β-CD : CuBr : PMDETA : TMSPMA are 1:21:21:21$\times$200). The mixture was sonicated until the solids were fully dissolved. Then the ampule was quickly sealed and degassed by three freeze-thaw cycles. The ampule was placed in a 50° C oil bath for 20 min and then cooled by liquid nitrogen to completely stop the reaction. The product was diluted by anhydrous dichloromethane, purified by a neutral alumina column and then precipitated by adding anhydrous petroleum ether. The final sticky product was dried in a vacuum oven for 4 hours.

2.1.6 Preparation of Si/SiO_2 Nanoparticle

- Materials Used

Chemicals used in this step were synthesized star-like PTMSPMA, dioxane, and ammonia.

- Procedures

0.005 g of star-like PTMSPMA was fully dissolved in 10 ml dioxane, and 1 ml ammonia (cross-linking agent) was injected into the solution. The solution was stirred under room temperature for 2 days. A few drops of the solution was applied onto a clean silicon wafer and sintered in air (to get SiO_2 nanoparticle) or in argon (to get Si nanoparticle).

- Characterization

Transmission electron microscope was employed to characterize the size of cross-linked PTMSPMS nanoparticles, and atomic force microscope was used to measure the size of the SiO_2 nanoparticles. TEM samples were prepared by applying three drops of above-mentioned solution onto a carbon coated copper TEM grid with 300 meshes, and checked in TEM after solution evaporated. The silicon wafer with sintered nanoparticles was directly used as the AFM sample.

2.2 Results and Discussion

2.2.1 Preparation of Initiator

- Experimental Procedures

The azeotropic distillation is based on the fact that the mixture of toluene and water has a lower boiling point than pure water. This is because the addition of toluene alters the molecular interactions in water and affects the activity coefficient of the mixture. This method is used to dehydrate β-CD.

The mechanism of β-CD bromination (esterification) is depicted in Figure 6. The reasons for using NMP as the reaction solvent are: first, NMP can dissolve β-CD; second, it doesn't react with 2-bromoisobutyryl bromide; and third, it can absorb HBr released during the reaction. The addition of 2-bromoisobutyryl bromide into the β-CD solution must be handled in cold environment to reduce fast reaction rate and to prevent violent reactions.

HBr can be further removed by reacting with $NaHCO_3$. Deionized water is used to remove NaBr and unreacted 2-bromoisobutyryl bromide in the mixture. The reaction mechanism of water and 2-bromoisobutyryl bromide is illustrated in Figure 15.

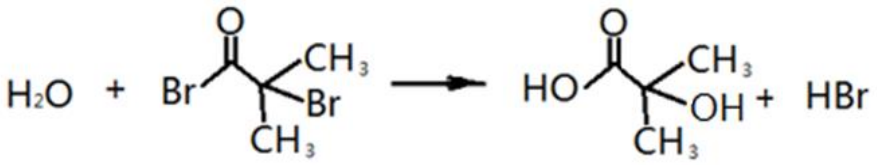

Figure 15: Reaction mechanism of water and 2-bromoisobutyryl bromide.

The precipitation of 21 Br-*β*-CD must be handled in cold environment because of the fact that cold hexane can precipitate 21 Br-*β*-CD while hot hexane dissolves it.

♦ Characterization

The successful esterification of *β*-CD is confirmed by ^{1}H NMR, as shown in Figure 16. Peak a (δ =3.5-5.5) was determined by the residual β-CD, and peak b (δ =1.8-2.2) was attributed to the methyl protons of 21 Br-β-CD. The locations of protons corresponding to peak a and peak b are represented in Figure 17, along with the ^{1}H NMR spectrum reported by Pang et al [11]. The peak locations highly resemble those reported by Pang et al [11].

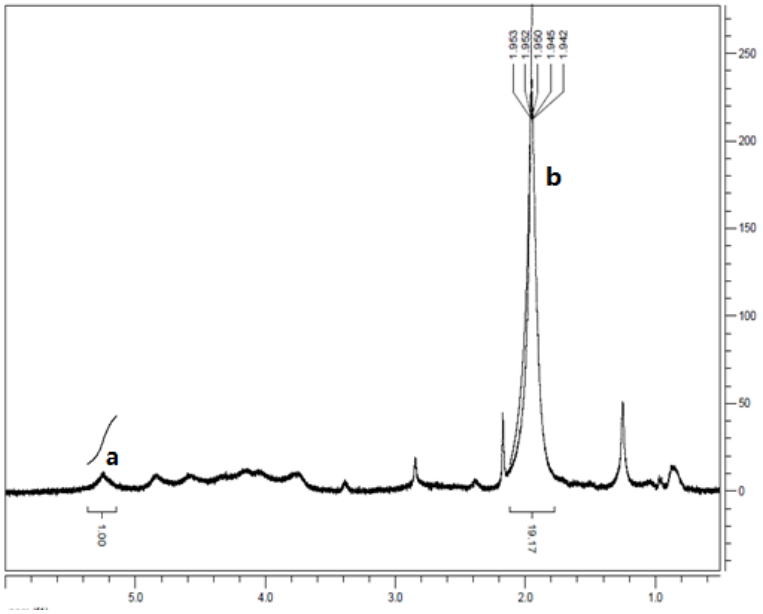

Figure 16: ^{1}H NMR spectrum of brominated *β*-CD. Area integration of peak a and peak b are 1 and 19.17, respectively.

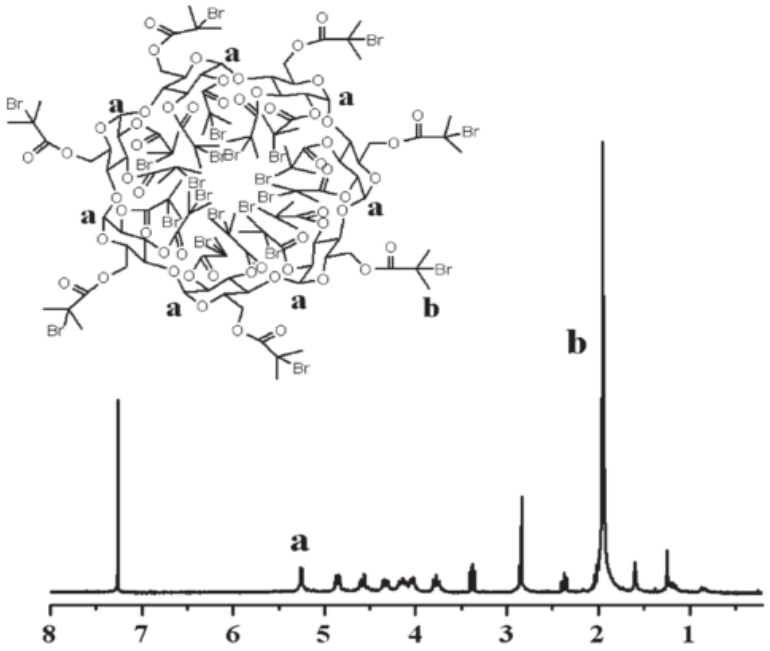

Figure 17: ^{1}H NMR spectrum of brominated β-CD reported in [11].

From Figure 17, it is evident that 21 Br-β-CD possesses 7 protons corresponding to peak a and 126 (6×3×7) protons corresponding to peak b. Type a protons are located on the original β-CD structure, while type b protons are located on the methyl groups of 2-bromoisobutyryl bromide. By calculating the number ratio of these two kinds of protons, the esterification efficiency can be determined:

$$\text{Efficiency} = \frac{\text{Area}_\text{b}}{18\times\text{Area}_\text{a}} \times 100\% \qquad \text{eq. 20}$$

where Area_a and Area_b are the integral areas of peak a and peak b, respectively. The area integration under the peak in NMR spectrum approximates the number of the proton corresponding to this peak. By a simple calculation, esterification efficiency is $\frac{19.17}{18\times1} = 1.065 \approx 1$. Since efficiency cannot be larger than one, the result might due to possible integration error. Also the calculation based on the NMR spectrum is not accurate enough and it just serves as a rough estimation. The esterification efficiency approximated to one suggests a complete conversion.

2.2.2 Preparation of Star-Like PtBA-*b*-PS Template

- Experimental Procedures

Successful polymerization requires completely dissolution of solids in solvents and completely removal of air in the system. The presence of oxygen greatly reduces the reactivity of radicals and thus affects the polymerization rate. For any undissolved solids, air is possible to remain inside the solids and is difficult to be removed. Thus, care must be taken during the freeze-thaw cycles to avoid air leakage.

The precipitator ratio (amount of methanol to that of water) and the amount of precipitator greatly affect the precipitation results. Multiple precipitations are thus necessary in order to completely remove homopolymers.

- Characterization
  - Synthesis of Star-like PtBA

Molecular weight of PtBA was checked by GPC. Figure 18 shows the molecular weight distribution of the product after purifications. The horizontal axis of the diagram represents time (min), and the vertical axis represents signal strength (mV). Two peaks are clearly resolved in the curve representing first precipitation: the peak appeared earlier corresponds to the star-like PtBA, while the peak appeared later corresponds to homopolymer PtBA. The goal of purification is to completely remove the homopolymer. The molecular distributions after third precipitation and fifth precipitation, respectively, are also depicts in Figure 18. The second peak is observed to be reduced after repeated precipitation, indicating successful removal of homopolymer.

It is observed that the peaks corresponding to the star-like PtBA are located at different evolution times (molecular weights), and there is no obvious trend in the shifting. There are several explanations for this measurement error: first, the GPC measurements were not conducted on the same day, so the GPC column pressure and temperature may fluctuate slightly. Since each precipitation took about one day, it was

not possible to conduct the measurement within a short period of time. Second, the concentrations of the tested samples were not exactly the same (5 mg/ml ± 1mg/ml). The peak was observed to shift to the right under higher concentration and shift to the left under lower concentration. It is worth mentioning that the intensity of each measurement is scaled such that the peak intensities corresponding the star-like polymers are approximately the same.

The M_n of the final product is about 123,900 g/mol (5,900 g/mol for each of the 21 arms), and the PDI (M_w/M_n) is about 1.12. The molecular weight measured may not be accurate because the shape of the star-like polymers is far different from that of the calibration reference – linear polystyrenes. Nevertheless, PDI measured by GPC is reliable. A PDI of 1.12 indicates uniform chain lengths of the 21 arms and entails a spherical shape of the star-like polymer.

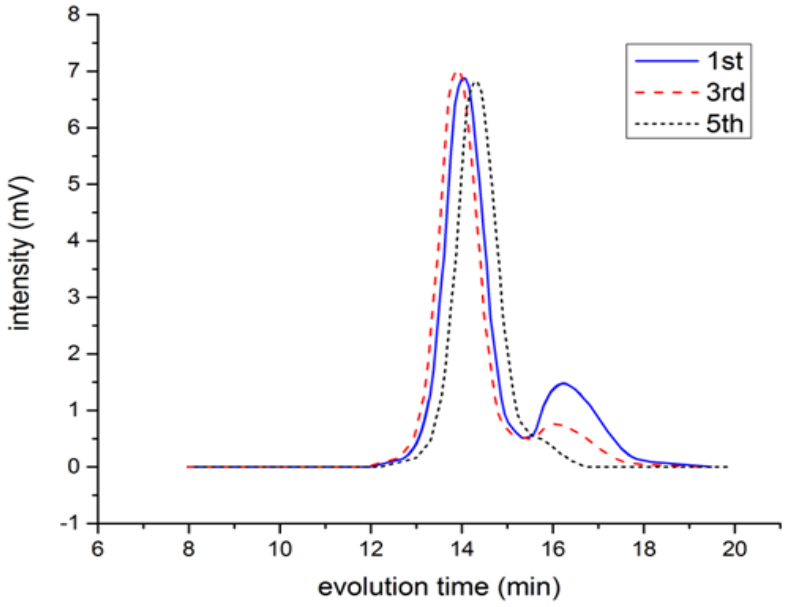

Figure 18: Molecular weight distribution of star- like PtBA after the first precipitation, the third precipitation and the fifth precipitation.

- Synthesis of Star-like PtBA-*b*-PS

The molecular weight distributions of PtBA-*b*-PS after precipitations are shown in Figure 19. The first peak of each curve manifests the star-like PtBA-*b*-PS, while the

second peak indicates the homo-polystyrene. Appropriate precipitator ratio (the amount of methanol to the amount of water) has a great impact on the purification results. Several precipitator ratios (1:0, 1:1, 2:1 and 1:2) were tried and only pure methanol can remove the homo-polystyrene in this system. The ratio may vary for other systems and a successful purification requires repeated trials. No more precipitation was performed after the fifth trial due to the limited amount of product remained. The effect of the homo-polystyrene is negligible in the subsequent synthesis, and the reason will be explained in the following section. The average M_n is approximately 196,800 g/mol, and the average PDI is about 1.25. it can be concluded that the M_n of the second block PS for each of the 21 arms is approximately 3500 g/mol ($\frac{196800-123900}{21}$ g/mol). Compared with the single-arm molecular weight of PtBA (~5,900 g/mol), the ratio of chain length PtBA : PS is approximately 1.7. It is noted that the template with this chain length ratio is effective to make nanoparticles in the following steps.

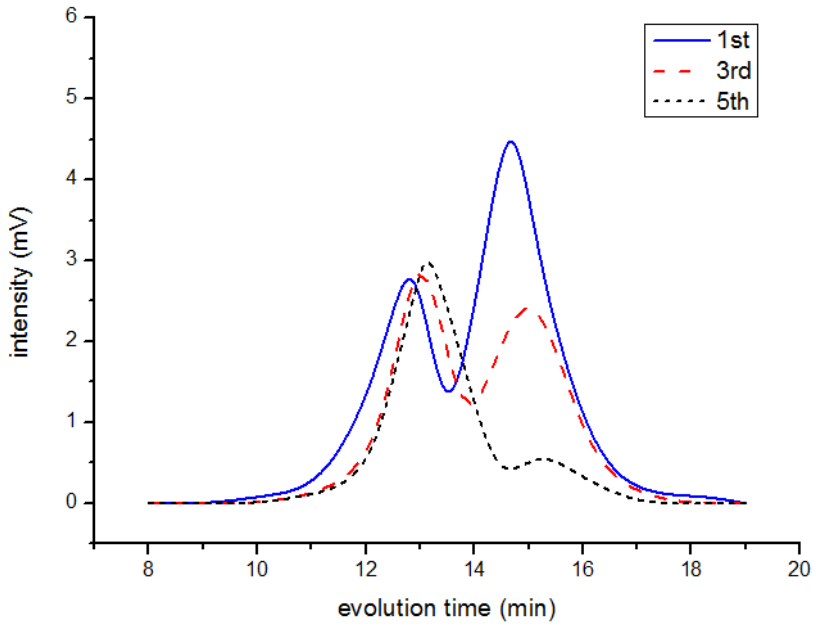

Figure 19: Molecular weight distribution of star- like PtBA-*b*-PS after the first precipitation, the third precipitation and the fifth precipitation.

2.2.3 Hydrolysis of PtBA

PtBA block in the synthesized PtBA-*b*-PS needs to be hydrolyzed to poly(acrylic acid) (PAA) because it is PAA that exerts strong coordination bonding with metals. The hydrolysis process is activated by a strong acid, such as trifluoroacetic acid, and the process is illustrated in Figure 20.

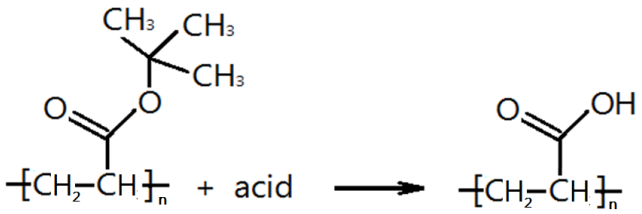

Figure 20: Hydrolysis of PtBA to PAA.

The solvent, CH_2Cl_2, dissolves PtBA-b-PS and homopolymer PS, and as hydrolysis takes place, PAA will precipitate out and can be collected at the end of the process. Therefore, PS that was not completely removed in the previous step did not affect the hydrolysis process and template formation.

2.2.4 Preparation of Fe_3O_4 Nanoparticle

The iron chloride hydrates react with PAA in the scheme manifested in Figure 21. The amount of $FeCl_2 \cdot xH_2O$ added should be in excess to avoid oxidation, as Fe (II) is unstable at ambient environment. Oxidation is further prevented by introducing argon during the reaction. The amount of $FeCl_3 \cdot xH_2O$ added determines the final amount of the Fe_3O_4 nanoparticles, as the ratio of reacted $FeCl_2$ and $FeCl_3$ is 1:2. The addition of ammonia produces $Fe(OH)_2$ and $Fe(OH)_3$ which are further decomposed into Fe_3O_4 under heat. Aging at higher temperature allows the atoms in Fe_3O_4 lattice to diffuse and

reconstruct, giving rise to a more uniform crystalline structure. The excess $FeCl_2 \cdot xH_2O$ added is dissolved in ethanol, while the nanoparticles are dissolved in toluene.

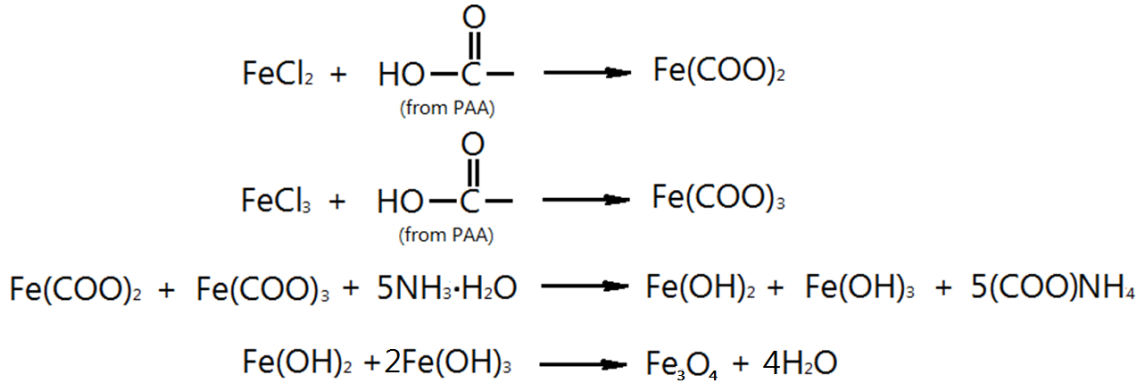

Figure 21: Reaction mechanism of $FeCl_2/FeCl_3$ with PAA.

TEM image of synthesized Fe_3O_4 nanoparticles is shown in Figure 22. It is observed that the sizes of nanoparticles are uniform with an average diameter of 10 nm. It is clearly resolved that the nanoparticles are separated from each other, confirming the presence of PS ligands that facilitate the separation of Fe_3O_4 nanoparticles.

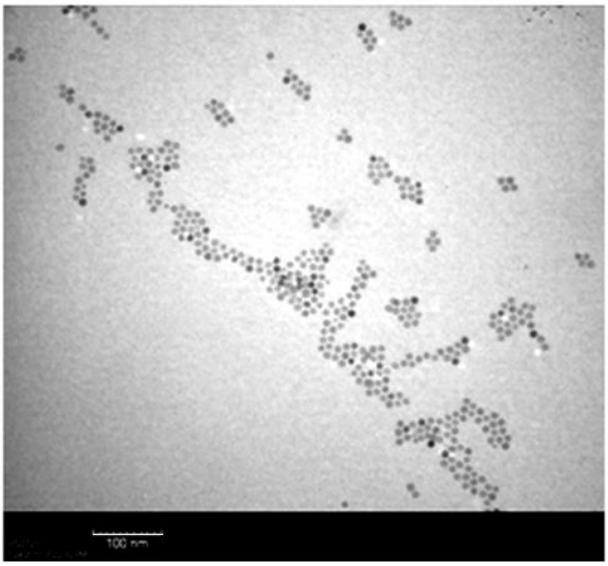

Figure 22: TEM image of Fe_3O_4 nanoparticles.

2.2.5 Preparation of Star-Like PTMSPMA Template

The reaction mechanism of synthesizing star-like PTMSPMA is depicted in Figure 23. Due to the nature of the monomer TMSPMA, ATRP reaction took place vigorously and a large molecular weight of resulting polymer may be obtained in a short time. 50° C was found to be the optimum reaction temperature, below which the reaction was barely initialized and above which the reaction took place too fast. Reaction time was controlled at 20 min in order to get desired molecular weight. The synthesized macromolecule consists of 21 arms and each arm possesses n Si-contained branches. The presence of vast amount of Si makes the system sensitive to heat and moisture. All the chemicals used in macromolecule synthesis and purification process must be desiccated to prevent Si network from cross-linking at this stage. Care must also be taken during chemical transfers and freeze-thaw cycles. The product should not be placed in the vacuum oven for over 4 hours and the temperature of the oven should be strictly less than 50° C. Note in order to get monodispersed nanoparticles in the end, a second block of PS (oil-soluble) or PEO (water-soluble) should be grafted to the end of Si-rich arms. But due to the difficulty of moisture removal and sensitivity of the Si network to heat, this step was neglected.

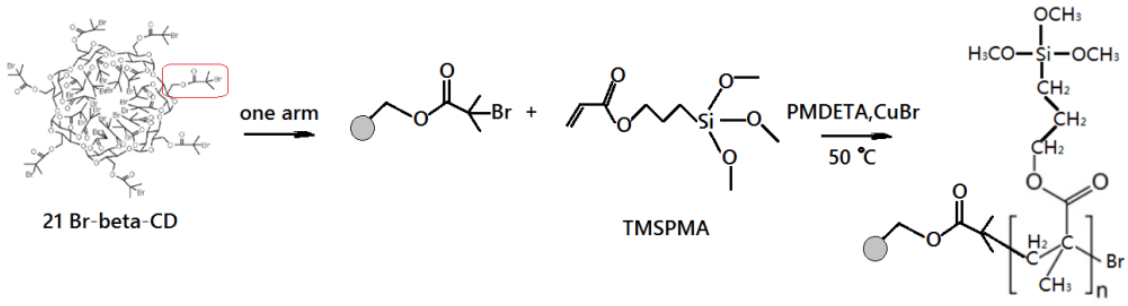

Figure 23: Reaction mechanism of synthesizing star-like PTMSPMA.

The GPC spectrum of star-like PTMSPMA is displayed in Figure 24. The average M_n is 111,700 g/mol or 5,300 g/mol per arm. PDI is 1.10. The spectrum exhibits a well resolved single peak with a moderate asymmetry. A slight shoulder is observed corresponding to the high molecular weight fraction, which corresponds to the coupling of the star-like polymers. An example of the coupling is two β-CD cores connected by one polymer chain, as indicated by the inset of Figure 24. From the GPC spectrum, the amount of coupling was very small and its effect is negligible.

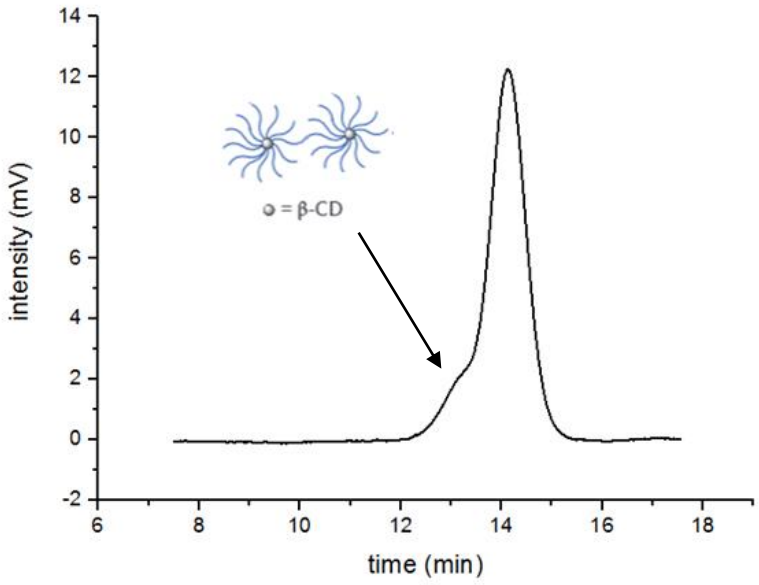

Figure 24: GPC spectrum of star-like PTMSPMA.

2.2.6 Preparation of Si/SiO_2 Nanoparticle

Ammonia ($NH_3 \cdot H_2O$) was added to facilitate the cross-linking of Si-based branches. The aim of cross-linking is to transform the soft polymer branches into rigid interconnected network. Without cross-linking, the final particles after sintering would collapse, resulting in a flat-pie shape instead of a 3-dimensional spherical shape. Figure 25 shows the silsesquioxane network formed between two Si-rich branches: the

tetrahedral SiO_4 units reduce the flexibility of branches and serve as the scaffold of the system.

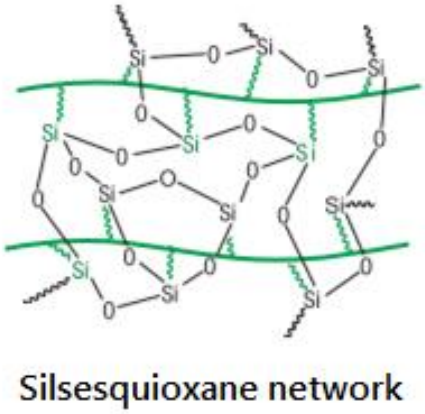

Figure 25: Si-based network obtained after cross-linking, reproduced from [12].

Ammonia needs to be in a small quantity (1 ml is used) and it needs to be added slowly while the solution is stirred vehemently. This is because without the outer capping (PS or PEG), macromolecules tend to aggregate. If a cluster of molecules meet a large amount of ammonia, they would cross-link with each other and form a large agglomeration. TEM image of polymeric nanoparticles after cross-linking (before sintering) is shown in Figure 26 ((A) low magnification, and (B) high magnification). The particle size is approximately 20 nm. The impurities in the background are attributed to the lack of purification after the process of cross-linking. The impurities may consist of small amount of homopolymer PTMSPMA. This is due to the fact that the C-Si bonds in the branches of PTMSPMA are easy to break under the basic condition (under the environment of ammonia). Since a small amount (0.005 g) of PTMSPMA was used, it is difficult to obtain noticeable amount of product if purification was conducted. Figure 27 (A) presents the agglomeration of a failed experiment, but there still exist single nanoparticles with diameter around 20 nm, as shown in Figure 27 (B). The reason for agglomeration is the addition of a relatively large amount of ammonia. The background

of Figure 26 has fewer impurities, and this is probably due to the fact that the polymeric clusters absorb surrounding chemicals in the way described as Ostewald ripening.

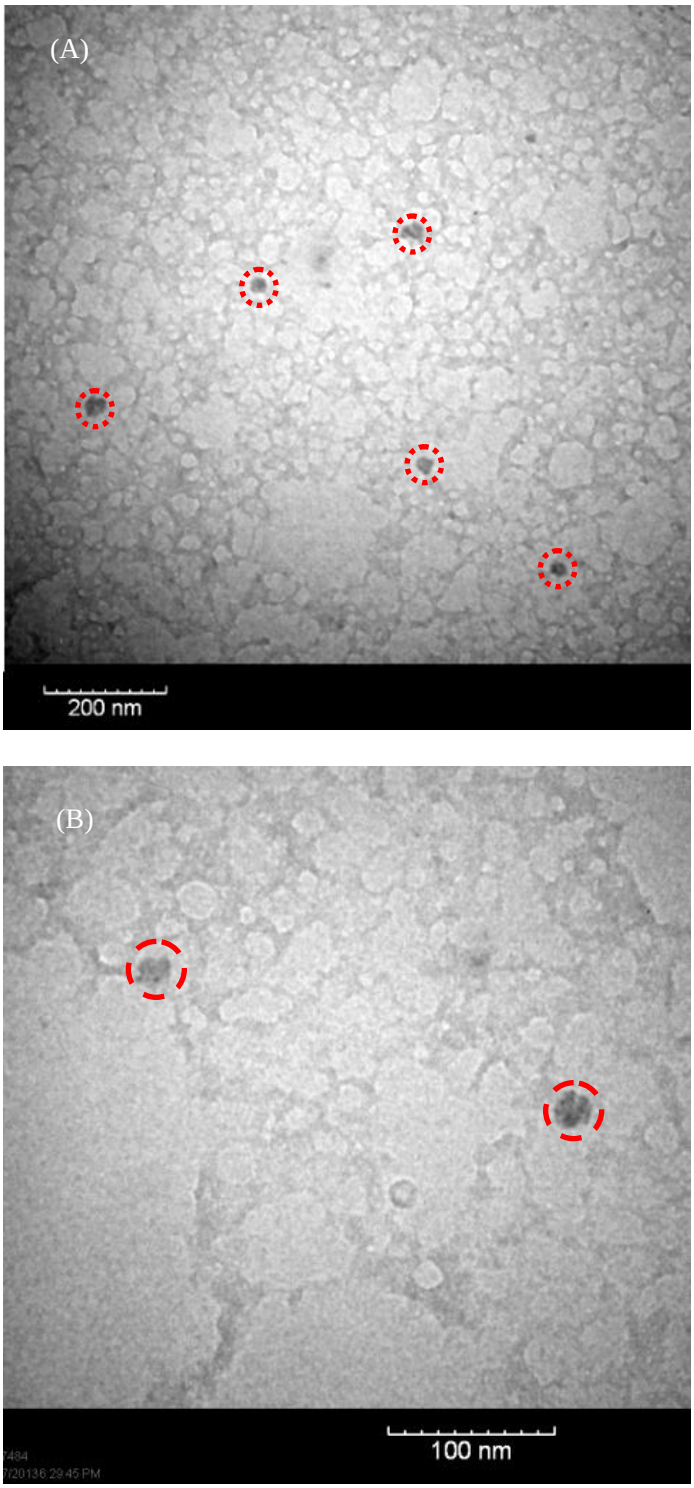

Figure 26: TEM images of polymeric nanoparticles after cross-linking under different magnifications.

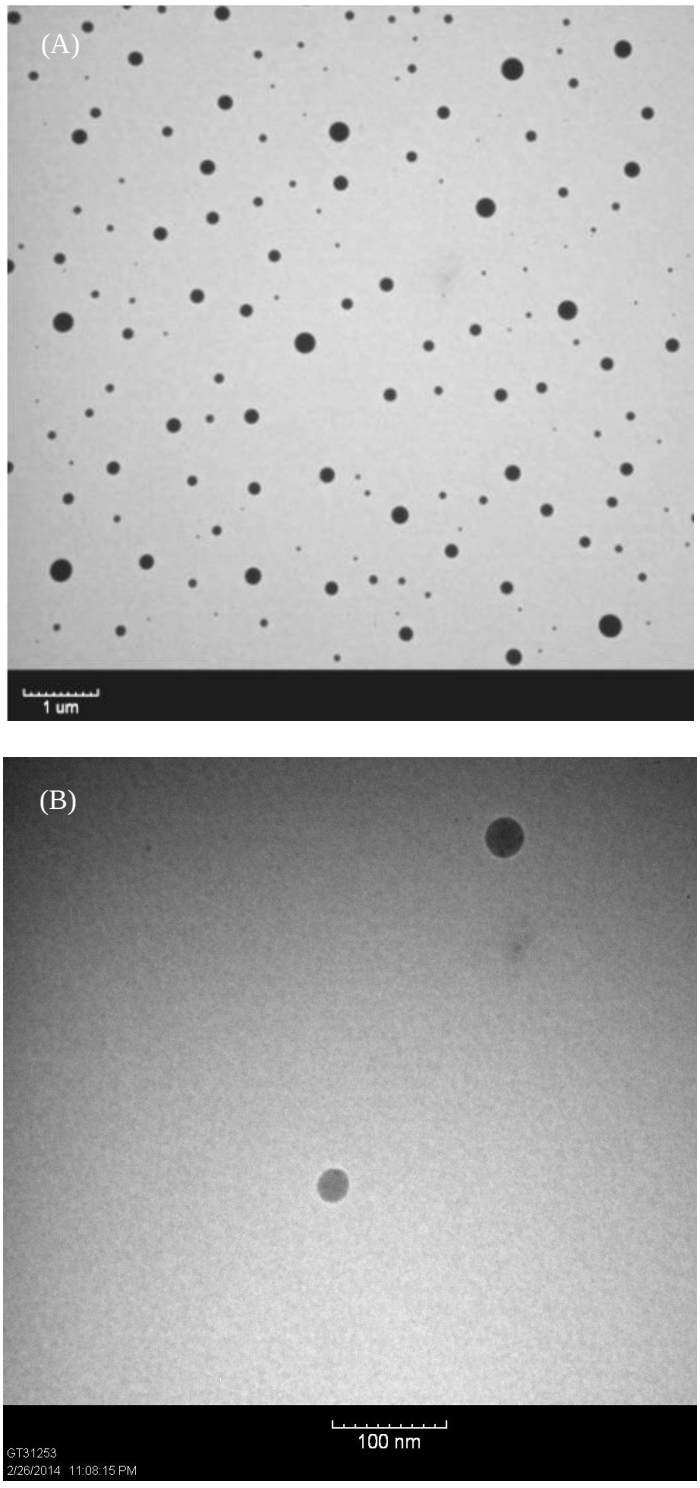

Figure 27: TEM images of polymeric clusters after cross-linking under different magnifications.

Figure 28 shows a portion of the AFM image of SiO_2 nanoparticles after the sintering process (in air). The histogram presented in Figure 29 shows the distribution of nanoparticle sizes. It is clear that 40nm is the most common diameter. Compared with the average diameter acquired from TEM image (20nm), the diameter measured by AFM is larger due to the effect given by the non-deconvoluted AFM tip. The height of nanoparticle measured by AFM was about 14nm (<20nm), indicated by the inserted figure in Figure 28. This is due to the fact that all the organic contents are removed after sintering, and thus the size of the inorganic components left behind should be smaller.

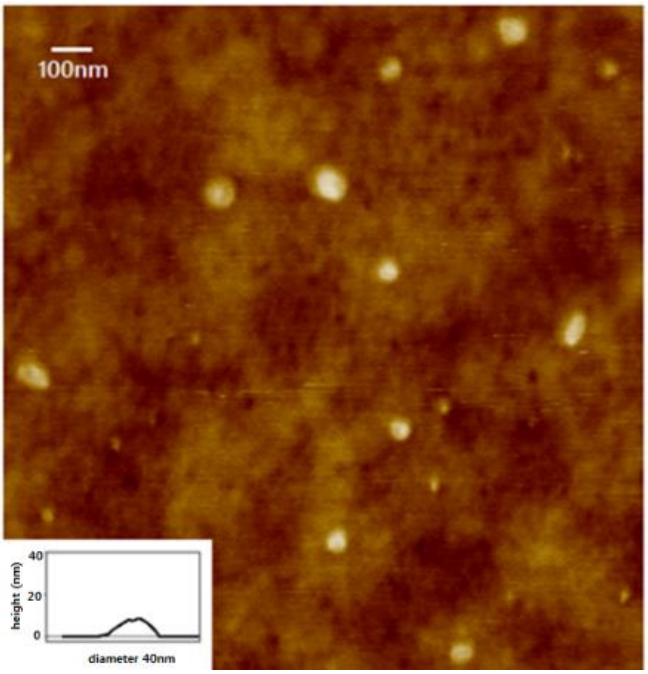

Figure 28: AFM image of SiO_2 nanoparticles. Inset: vertical scan of a nanoparticle with diameter of 40 nm.

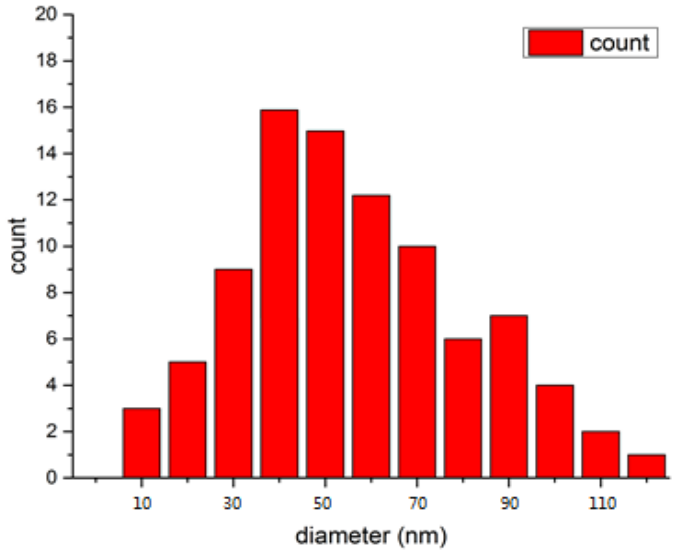

Figure 29: Histogram of SiO_2 nanoparticle sizes.

2.3 Conclusions

The use of polymeric template can serve as a versatile tool for the nanoparticle fabrication. In this thesis, two types of templates are introduced, namely, star-like PAA-*b*-PS for Fe_3O_4 nanoparticle synthesis and star-like PTMSPMA for SiO_2 nanoparticle synthesis. PAA-*b*-PS can also be used to produce $PbTiO_3$, TiO_2, ZnO, Au, etc [2]. By modifying the polymer chain types, nanoparticles with hollow and core-shell architectures can also be crafted [2]. The synthesized nanoparticles possess uniform sizes and monodispersity. Improvement can be made on SiO_2 nanoparticles by adding capping ligands, such as PS or PEG, to the end of the PTMSPMA templates in order to prevent agglomeration. We envision that Fe_3O_4 nanoparticles exhibit superparamagnetic properties due to their small dimensions and they can be used in wide applications, such as magnetic resonance imaging, magnetic storage, and catalysis. Si nanoparticles can be used in fuel cell layers, lithium ion battery anodes as a replacement of carbon [13], and photovoltaic cells as fluorescing centers [14]. If made hollow, SiO_2 nanoparticles can also be used as drug delivery carriers.

CHAPTER 3

SIMULATION

Nanoparticles made of noble metals, such as Au and Ag, have been widely used in many application due to their characteristic absorption in visible light range. Simulation of the optical properties of these noble metals is helpful in experimental design and validation. In this chapter, simulation of optical properties of Au nanoparticle and Au/TiO_2 core-shell nanoparticle are scrutinized. Simulation was carried out using COMSOL Multiphysics® 4.4 under the *Radio Frequency*, *Electromagnetic Waves, Frequency Domain* module.

3.1 Simulation Setups

3.1.1 Simulation of Optical Properties of Au Nanoparticle

The optical property of a gold nanoparticle dispersed in water was simulated by COMSOL. The interface used in this simulation was *Electromagnetic Wave, Frequency Domain* (emw) under the module Radio Frequency. Study was carried out in 2D under frequency domain. Parameters were defined as shown in Table 1. Two parameter interpolations were done for the material gold, one for the real part of permittivity ε'_{Au} and the other for the imaginary part of permittivity ε''_{Au}. The data for the interpolations were obtained from Johnson and Christy [15] (Table 2). After the model was constructed and materials were applied to appropriate domains, the *Perfectly Matched Layer* (PML) and *Scattering Boundary Condition* was defined as schematically shown in Figure 30 (A). *Mapped mesh* was applied to the PML domain and the remaining structure was constructed in *free triangular mesh* (Figure 30 (B)). The *Scattering Boundary Condition*

was defined on the outer boundary of the PML. One "*Wave equation, Electric*" physics is added under the "*Electromagnetic Waves, Frequency Domain*" interface and *dielectric loss* was set as the electric displacement field model for all domains (both gold and surrounding water). Under the study, *parametric sweep* was set from 400 nm to 700 nm with a step size of 10 nm, and a sweep from 410 nm to 430 nm with step size 1 nm was carried out to locate the absorption peaks.

Table 1: Parameters for the simulation of the Au nanoparticle.

Parameter name	Expression	Notes
wl ($\boldsymbol{\lambda}$)	400[nm] – 700[nm]	Wavelength of background light
f	c_const/wl	Frequency of background light: $\boldsymbol{f = \frac{c}{\lambda}}$
k	2*pi/wl	Wave number of background light: $\boldsymbol{k = \frac{2\pi}{\lambda}}$
WaterRe	1.7822	Permittivity of water, real part: $\boldsymbol{\varepsilon'_{water}}$
WaterIm	2.67e-9	Permittivity of water, imaginary part: $\boldsymbol{\varepsilon''_{water}}$
Watersigma	2*pi*f*WaterIm*8.854e-12[F/m]	Electric conductivity of water: $\boldsymbol{\sigma_{water} = 2\pi f \varepsilon_0 \varepsilon''_{water}}$
r	10[nm], 20[nm], 30[nm], 40[nm]	Radius of nanoparticle
t_surr	wl/2	Thickness of surrounding media
t_pml	wl/4	Thickness of PML
Ausigma	2*pi*f*AuIm(wl)*8.854e-12[F/m]	Electric conductivity of gold, using interpolation function AuIm(wl)

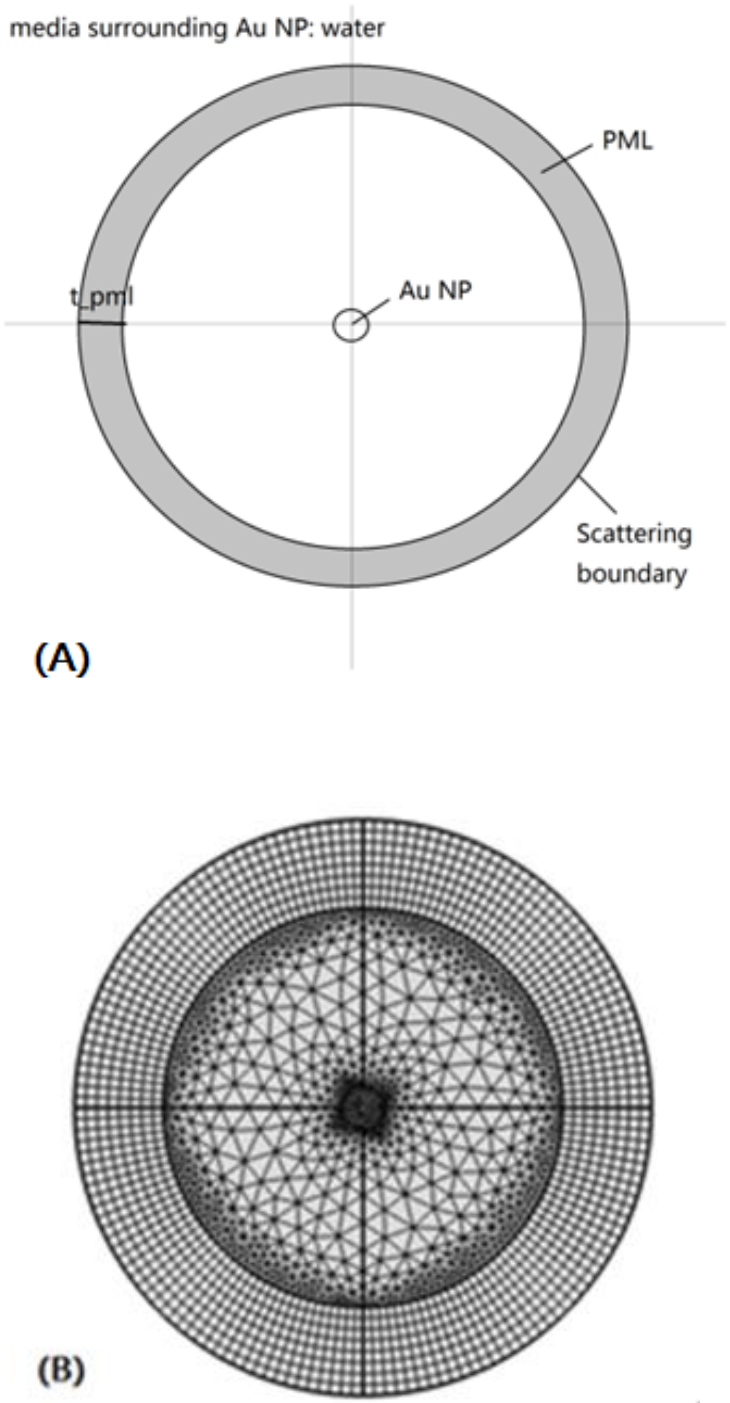

Figure 30: (A) Schematic diagram showing the construction of the model, and (B) screen shot of 2D meshing construction from COMSOL.

Table 2: Permittivity of gold [15].

Wavelength (nm)	$\varepsilon'_{\mathrm{Au}}$	ε''_{Au}
400	-1.658	5.7354
410	-1.6912	5.7218
420	-1.6983	5.6908
430	-1.6925	5.6512
440	-1.7242	5.4773
450	-1.7562	5.2986
460	-1.7342	5.0858
470	-1.7066	4.8737
480	-1.9213	4.4802
490	-2.153	4.0595
500	-2.5676	3.6391
510	-3.2472	3.1689
520	-3.8901	2.632
530	-4.5461	2.4577
540	-5.2313	2.2874
550	-5.9311	2.097
560	-6.5818	1.9836
570	-7.2587	1.8497
580	-7.9617	1.6955
590	-8.6647	1.6069
600	-9.3875	1.5292
610	-10.137	1.4407
620	-10.874	1.353
630	-11.548	1.2821
640	-12.241	1.2048
650	-12.953	1.1209
660	-13.682	1.0356
670	-14.358	1.044
680	-15.051	1.0516
690	-15.76	1.0584
700	-16.486	1.0643

Table 3: Refractive index of TiO_2 [16].

Wavelength (nm)	n_{TiO_2}
400	--
410	--
420	--
430	2.8717
440	2.84033
450	2.81257
460	2.78785
470	2.76571
480	2.74577
490	2.72773
500	2.71135
510	2.69641
520	2.68273
530	2.67018
540	2.65861
550	2.64794
560	2.63805
570	2.62887
580	2.62033
590	2.61237
600	2.60494
610	2.59799
620	2.59147
630	2.58534
640	2.57959
650	2.57417
660	2.56905
670	2.56422
680	2.55966
690	2.55533
700	2.55124

3.1.2 Simulation of Optical Properties of Au/TiO_2 Core/Shell Nanoparticle

The optical property of Au/TiO_2 nanoparticle dispersed in water was simulated by COMSOL. The interface used in this simulation was *Electromagnetic Wave, Frequency Domain* (emw) under the module Radio Frequency. Study was carried out in 2D under frequency domain. Parameters were defined as shown in Table 2. An extra parameter was t_s, the thickness of shell layer. Apart from the interpolations for $\boldsymbol{\varepsilon'_{Au}}$ and $\boldsymbol{\varepsilon''_{Au}}$, the refractive index of TiO_2, $\boldsymbol{n_{TiO_2}}$, was interpolated with respect to wavelength, and the data was extracted from Devore [16] (Table 3). After the model was constructed and materials were applied to appropriate domains, the *Perfectly Matched Layer* (PML) and *Scattering Boundary Condition* was defined in the same way as the gold nanoparticle simulation. The mesh was set up as indicated in Figure 31. *Mapped mesh* was applied to the PML domain and the remaining structure was meshed in *free triangular mesh*. One "*Wave equation, Electric*" physics is added under the "*Electromagnetic Waves, Frequency Domain*" interface and *dielectric loss* was set as the electric displacement field model for all domains (Au, TiO_2 and surrounding water). Under the study, *parametric sweep* was set from 400 nm to 700 nm with a step size of 10 nm.

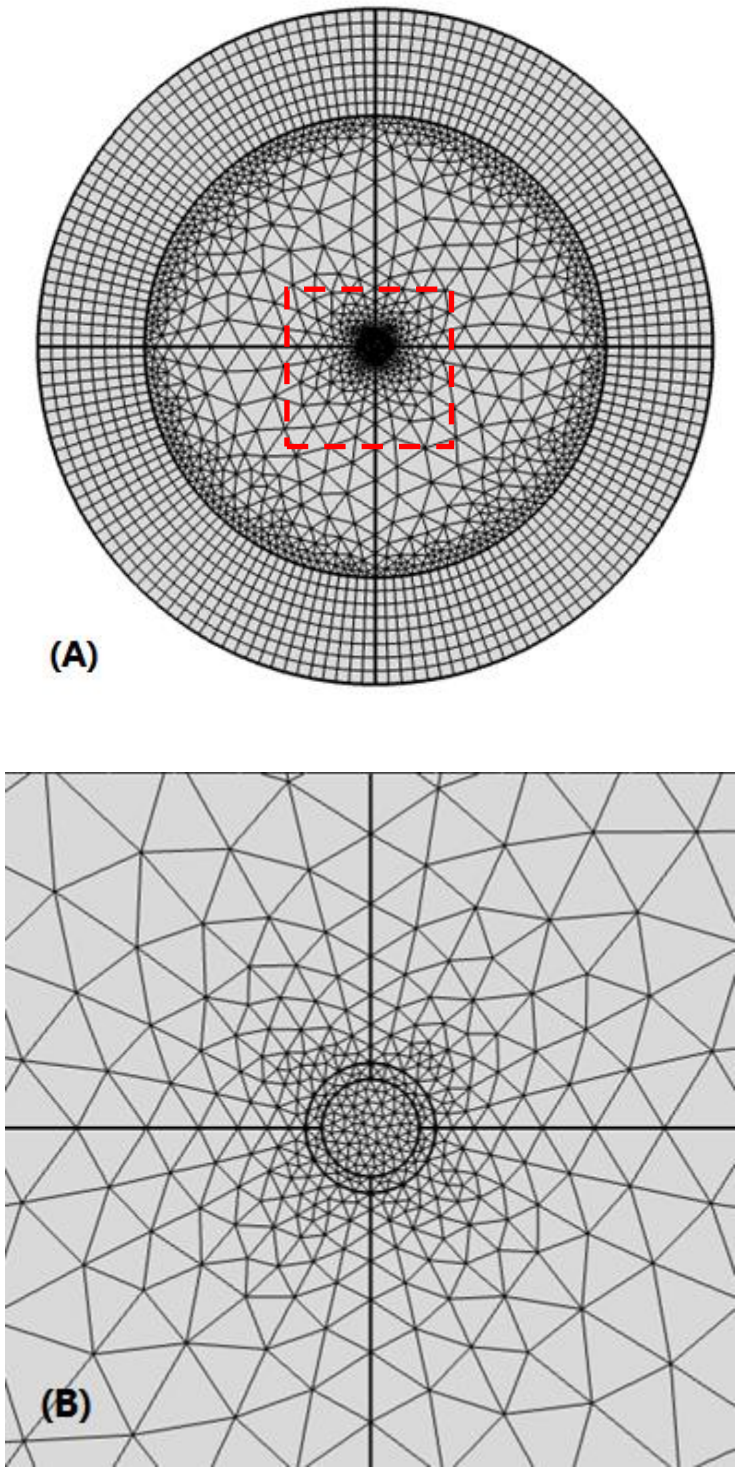

Figure 31: (A) Screen shot of 2D meshing construction from COMSOL. (B) Center region is enlarged. Note the core/shell structure at the center.

3.2 Results and Discussion

3.2.1 Simulation of Optical Properties of Au Nanoparticle

The scattering boundary condition generates a boundary transparent for both an incoming plane wave and a scattered outgoing wave normal to the boundary, while it blocks tangential waves at the boundary; the waves at oblique incidence is partially reflected. Perfectly matched layer (PML) absorbs all radiation with small reflections, and it is used to model an open boundary. The combination of scattering boundary condition and perfectly matched layers enable a relatively accurate simulation of infinite dimension even though the simulated domains are of limited volumes.

The meshes constructed in COMSOL are adjusted automatically based on the size of the structures. The meshes are finer for small and detailed features. This can be seen from Figure 29 and Figure 30, in which the meshes around small nanoparticles are finer while those in the water region are coarser. This mesh construction removes unnecessary calculations and increases the simulation speed.

Absorption spectrum was obtained by post-processing on simulated results. According to Equation 17, the absorption power consists of two parts: electric part and magnetic part. The magnetic contribution is usually too small to be considered. Therefore, the absorption power was calculated by volume integration of $\frac{1}{2}\boldsymbol{Re}(\mathbf{J_{tot}} \cdot \mathbf{E_{tot}^{*}})$ over nanoparticle volume. The expression:

real(0.5*(emw.Jx*conj(emw.Ex)+emw.Jy*conj(emw.Ey)))

was obtained by expanding $\frac{1}{2}\boldsymbol{Re}(\mathbf{J_{tot}} \cdot \mathbf{E_{tot}^{*}})$ into the corresponding vector components (there was no z component), and it was found to generate same result as the expression emw.Qe, which represents “electromagnetic power loss density”. The power loss was then calculated using emw.Qe for a given particle size under incident light with

wavelength from 400 nm to 700 nm. The absorption spectra of 10 nm, 20 nm, 30 nm and 40 nm gold nanoparticles are plotted in Figure 32.

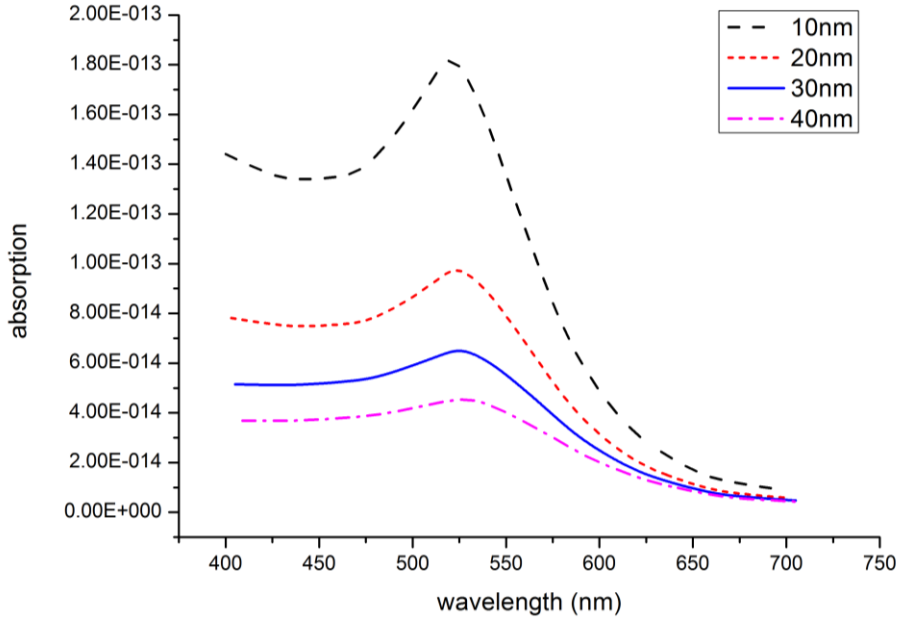

Figure 32: Simulated absorption spectra of gold nanoparticle with diameter of 10 nm, 20 nm, 30 nm and 40 nm, respectively.

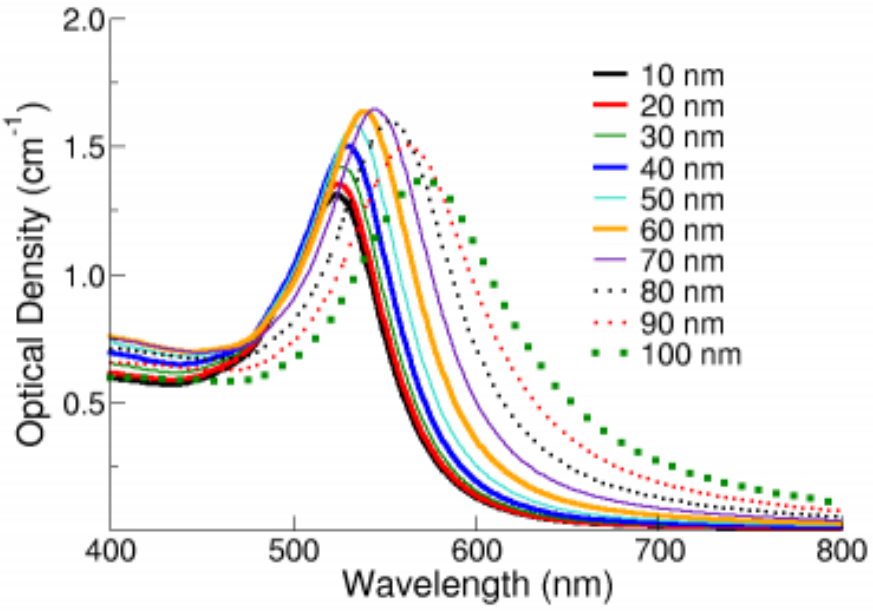

Figure 33: Spectra of NanoXact gold nanoparticles with diameters ranging from 10 - 100 nm [18].

By a detailed sweep, the absorption peaks for 10 nm, 20 nm, 30 nm and 40 nm gold nanoparticles were found out to be located at 520 nm, 523 nm, 525 nm and 529 nm, respectively. It is obvious that the absorption peaks are located at around 520 nm to 530 nm and shifts to longer wavelength when nanoparticle size increases. This phenomenon can be explained as follows. The incident electromagnetic wave is coupled into a surface plasmon at the nanoparticle surface, resulting in a surface plasmon band that is responsible for the absorption of electromagnetic energy. Since the absorption peak of Au nanoparticles is usually located at 500nm wavelength, green light is absorbed and thus the Au nanoparticle suspension appears red. The surface plasmon, or the collective oscillation of conduction band electron with incident radiation, is sensitive to the nanoparticle size due to the surface confinement. As the nanoparticle size decreases, the energy needed to excite the surface plasmon increases, giving rise to the absorption of light with shorter wavelength (higher energy) [17]. Compared with the measured absorption spectrum shown in Figure 33, the simulated results match the general trend but are different in intensity. This is because the simulation is only restricted to one nanoparticle, and the optical intensity scales with particle size. In contrast, a large concentration of nanoparticles is generally measured in real experiments, and therefore the intensities are comparable for various nanoparticle sizes.

The simulated optical field of a gold nanoparticle in x-y plane is shown in Figure 34. The background light was set as $\mathbf{E_b} = \boldsymbol{e}^{-\boldsymbol{jkx}}\hat{\mathbf{y}}$, that is, the waves propagate in the x direction and polarize in the y direction. The software solved the in-plane vector of the scattered electric field. It is observed that the optical field is polarized in the y direction, which agrees with the polarization of the incident plane wave. As explained before, this phenomenon is due to the collective oscillation of conductive electrons and incident photons.

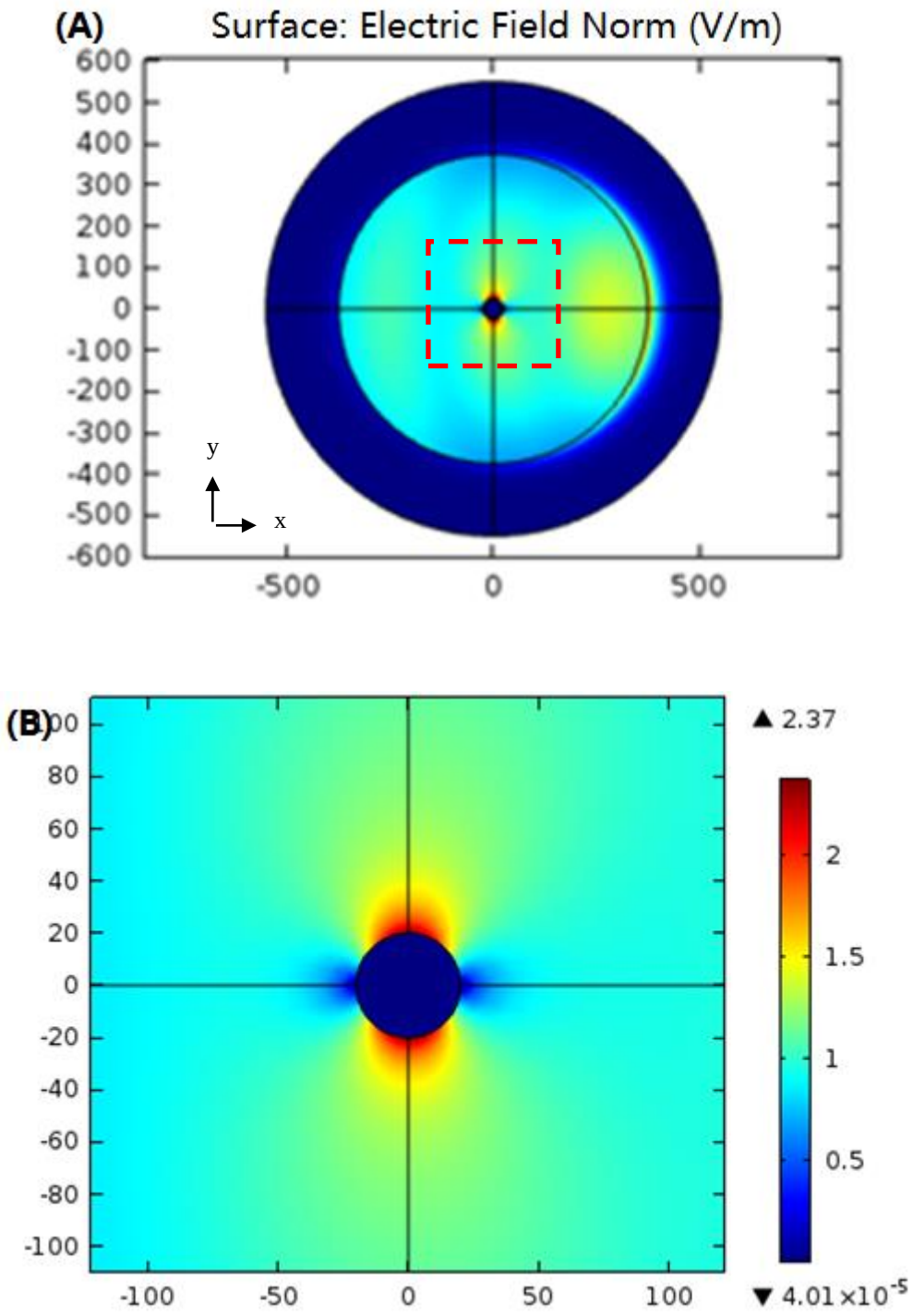

Figure 34: (A) Simulated optical field for a gold nanoparticle. (B) Center region is enlarged.

3.2.2 Simulation of Optical Properties of Au/TiO_2 Core/Shell Nanoparticle

Since the imaginary part of the permittivity of TiO_2 is very small, only the real part of the permittivity was used in simulation. This assumption is applicable as TiO_2, a semiconductor, doesn't possess a significant amount of mobile electrons. The refractive index of a general material is given by $\boldsymbol{n = \sqrt{\varepsilon_r \mu_r}}$, and $\boldsymbol{\mu_r \approx 1}$ at optical frequencies (400 nm – 700 nm), so $\boldsymbol{\varepsilon'_{TiO_2} = n^2_{TiO_2}}$. Since $\boldsymbol{\varepsilon''_{TiO_2}}$= 0, the electrical conductivity of TiO_2 was also set to zero.

Figure 35 compares the simulated absorption spectra of Au/TiO_2 nanoparticles with a fixed shell thickness 5nm and varied core radii (5 nm, 10 nm, 15 nm, and 20 nm). Compared to the absorption spectrum of pure Au nanoparticle (15 nm), the absorption peaks of Au/TiO_2 nanoparticles shift to longer wavelengths. As core radius increases, the absorption peak red shifts slightly. This simulation result is confirmed by experimental measurement (UV-vis) shown in Figure 36.

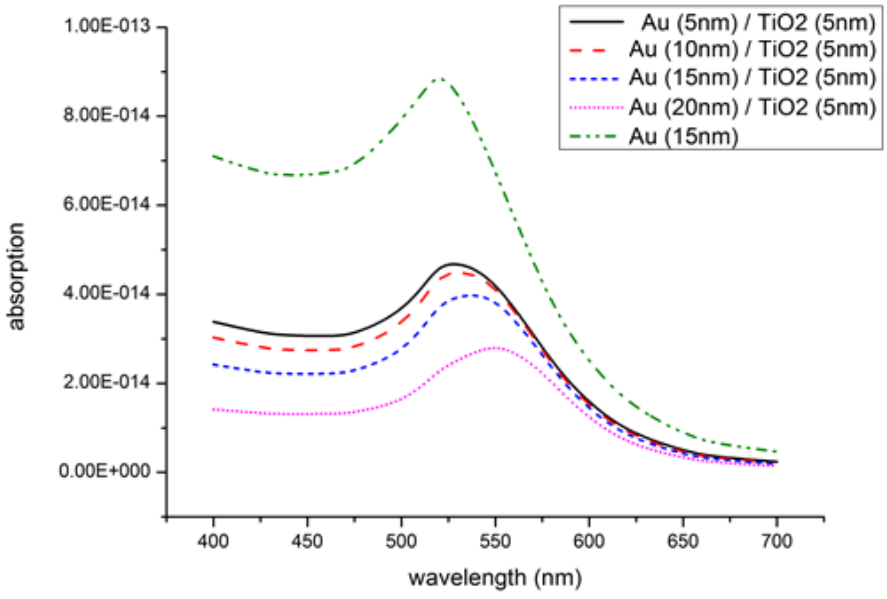

Figure 35: Simulated absorption spectra of Au/TiO_2 nanoparticles with a fixed shell thickness and varied core radii.

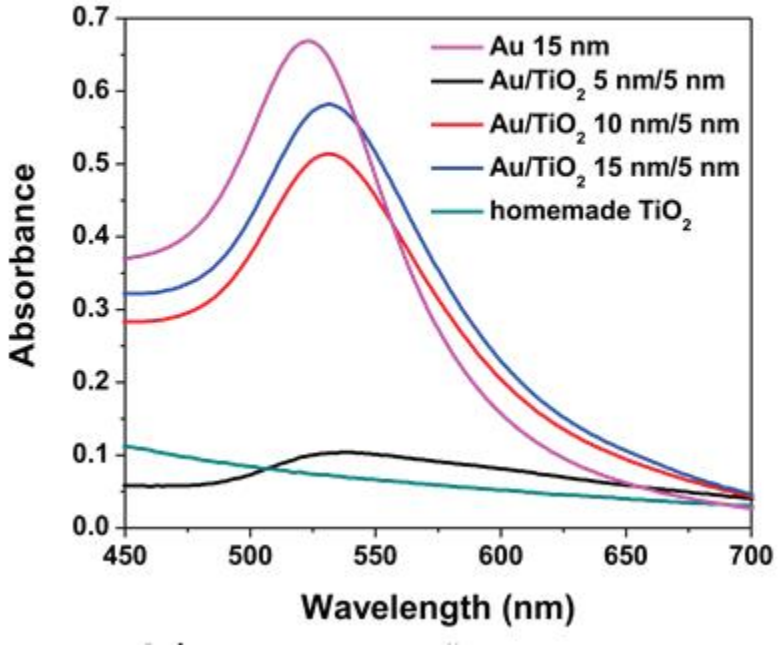

Figure 36: Experimental measurement (UV-vis) of Au/TiO_2 nanoparticles with a fixed shell thickness and varied core radii.

Since the electrical conductivity of TiO_2 is assumed to be zero, there is no resistive loss in the TiO_2 shell layer. Therefore, no absorption peak should be observed for pure TiO_2, as shown in Figure 36. What's more, the TiO_2 shell has negligible contribution to the resistive loss of Au/TiO_2 nanoparticles. As a result, the absorption peak shift of Au/TiO_2 nanoparticles should follow the same trend as exhibited in pure Au nanoparticle. The red shift of absorption spectrum of Au/TiO_2 (15 nm/5 nm) compared with that of pure Au (15 nm) is due to the change in permittivity of surrounding media: Au is surrounded by water in the pure Au nanoparticle, while Au is enveloped by TiO_2 in the Au/TiO_2 nanoparticle. This can be explained by the following equation [19]:

$$\omega_{SPR} \approx \frac{\omega_p}{\sqrt{1+2\varepsilon_m}} \quad \text{eq. 21}$$

where $\boldsymbol{\omega_{SPR}}$ is the surface plasmon resonance frequency, $\boldsymbol{\omega_p}$ is the plasmon frequency of the bulk metal ($\boldsymbol{\omega_p} = \sqrt{\frac{ne^2}{\varepsilon_0 m^*}}$, where n is the electron density, e is the electric charge, and $\boldsymbol{m}^*$ is the effective mass of electron), and $\boldsymbol{\varepsilon_m}$ is the permittivity of surrounding media. Since TiO_2 has a larger permittivity than water, the surface plasmon resonance frequency of Au/TiO_2 nanoparticle becomes smaller and the resonance wavelength becomes larger. The estimation given in Equation 21 can only qualitatively predict the trend of plasmon resonance frequency change, since it doesn't consider other factors such as the effect of nanoparticle size [19].

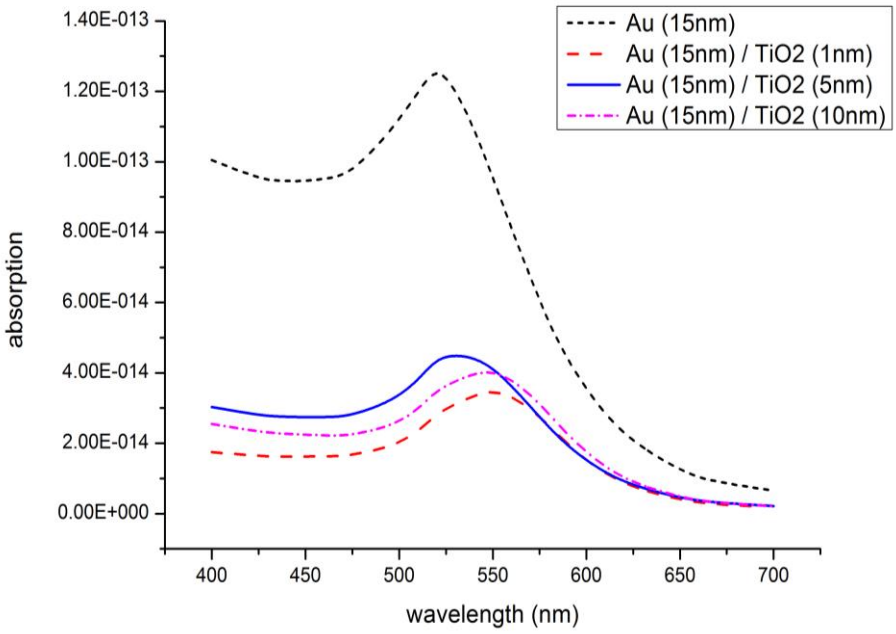

Figure 37: Simulated absorption spectra ofAu/TiO_2 nanoparticles with a fix core radius and varied shell thicknesses.

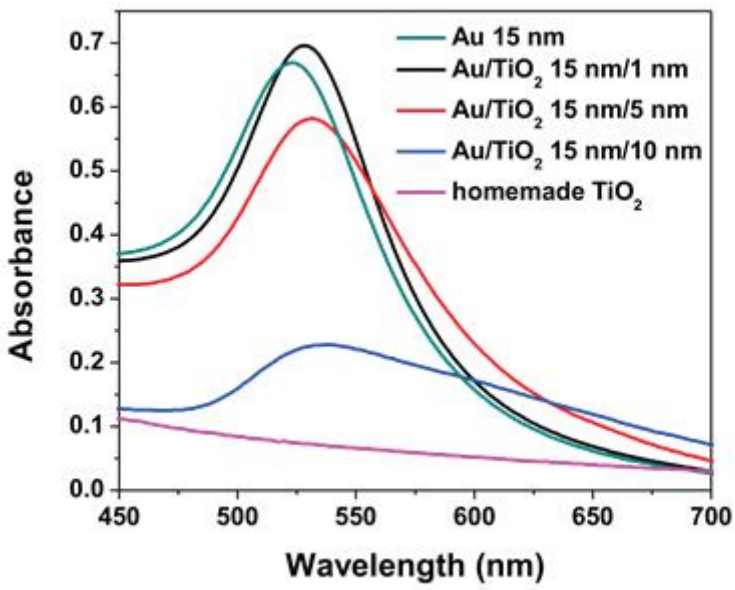

Figure 38: Experimental measurement (UV-vis) of Au/TiO_2 nanoparticles with a fix core radius and varied shell thicknesses.

Figure 37 shows the simulated absorption spectrum of Au/TiO_2 nanoparticles with a fixed core radius 15nm and varied shell thicknesses (1 nm, 5 nm, and 10 nm). Due to possible simulation error, there is no trend observed on peak shifting. Nevertheless, two results can be confirmed by experimental measurement shown in Figure 38. First, compared to the absorption spectrum of pure Au nanoparticle (15 nm), the absorption peaks of Au/TiO_2 nanoparticles slightly shift to longer wavelengths. As noted in the previous section, this is due to the change of surrounding media. Second, the peak locations are almost identical for nanoparticles with different shell thickness. Due to the limited set of experiments conducted, only TiO_2 shell thickness of 1 nm, 5 nm and 10 nm were examined. It is possible that for larger TiO_2 thickness, the absorption peak would demonstrate a noticeable shift to longer wavelength. This predication can also be proved by the experimental results provided in Liu et al [20] (Figure 39). The absorption peak location is correlated to the effective index of the overall core/shell nanoparticle. In Liu et al, it is found that the effective index of Au/TiO_2 (5 nm) and that of Au/TiO_2 (8 nm) are

identical, and the absorption peaks of these two cases are at the same location. It is shown that, as the shell thickness further increases, the effective index of the overall core/shell nanoparticle would increases, giving rise to the red shift of absorption peaks [20].

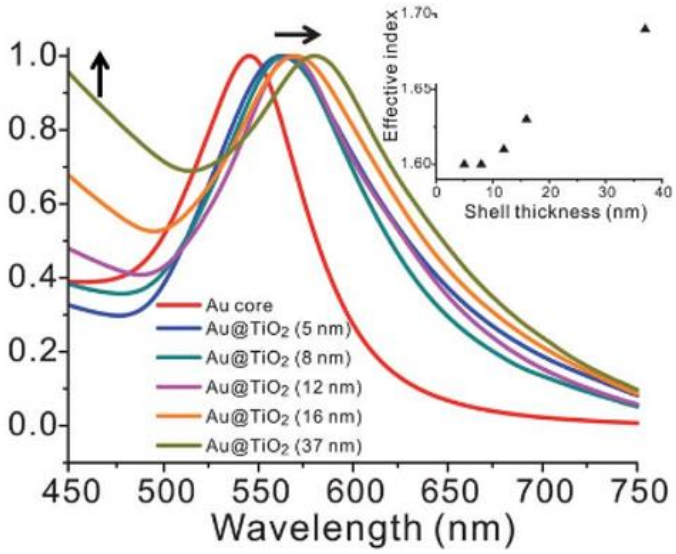

Figure 39: Absorption peaks of Au/TiO_2 nanostructures with different shell thickness, reproduced from [20].

The simulated optical field of Au/TiO_2 is shown in Figure 40. It is observed that the enhancement of local electromagnetic field on the outer surface of the TiO_2 shell due to the localized surface plasmonic resonance effect.

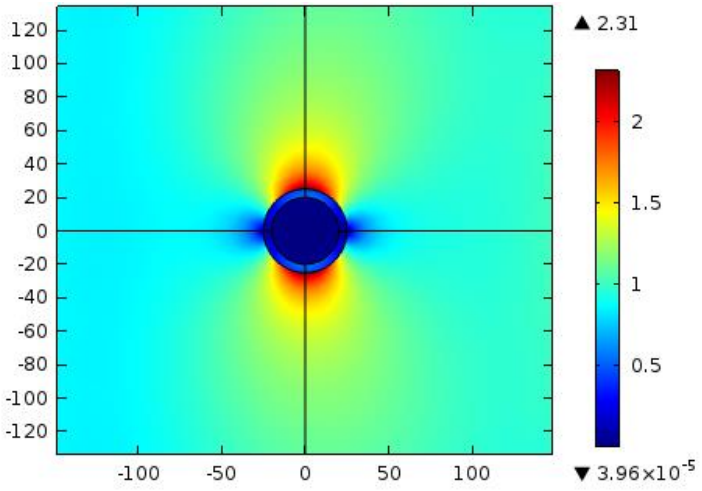

Figure 40: Simulated optical field of Au/TiO_2 nanoparticle.

3.3 Conclusions

The advantage of performing simulation is that it predicts and optimizes the results prior to conducting the experiments. Simulation can also be used to confirm experimental results and guide the experimental design and synthesis. It helps eliminating tedious and repeated works and accerlarating experimental progress.

The simulation conducted for this thesis can also be done in 3D. Since the nanoparticle possess axial symmetry, 2D calculation is accurate enough and time efficient. For more complicated structure, 3D simulation is prefered. The simulation results can be improved by modifying the parameters, e.g. the permittivity of surrounding water.

The optical properties of nanoparticles are influence by the surrounding media. If the surrounding media is changed, the absorption spectrum will be varied.

The localized surface plasmon resonance of gold nanoparticles is usually used to enhance optical absorption in solar energy harvesting, photonic, sensing and other applications. The Au/TiO_2 core shell nanoparticles are widely used in photocatalysis, water splitting, and dye-sensitized solar cell applications. In photocatalysis and water splitting applications, TiO_2 shell serves as a protecting layer to the gold core and also facilitates charge transfer. In solar cell applications, particularly the dye-sensitized solar cells in which TiO_2 is widely used as photo-anode, the TiO_2 shell leads to uniform dispersion of Au/TiO_2 nanoparticles in the TiO_2 matrix and also reduces interface resistance.

CHAPTER 4

CONCLUSIONS

4.1 Thesis Review

This thesis has studied the synthesis of plain nanoparticles and the simulation of plasmonic nanoparticles. In the synthesis part, Fe_3O_4 nanoparticles and SiO_2 nanoparticles are produced based on polymer templates with slightly different synthetic routes. Synthesis of Fe_3O_4 involves the preparation of PAA-*b*-PS polymer templates and the addition of $FeCl_2$/$FeCl_3$ precursors. In contrast, in the synthesis of SiO_2 nanoparticles, it relys on a single-step Si-based polymer template synthesis, and no extra precursors are needed. Nuclear magnetic resonance (NMR) is used to characterize 21 Br-β-CD. Gel premeation chromotography (GPC) is used to measure molecular weights of the resulting polymers. Atomic force microscopy (AFM) and transmittion electron microscopy (TEM) are used to evaluate the nanoparticle morphologies. In the simulation part, the optical properties of pure gold nanoparticle and Au/TiO_2 core/shell nanoparticle in water are simulated by COMSOL. The plasmonic near field map exhibits the polarization corresponding to that of the incident plane wave. As the size of gold nanoparticle increases, the absorption peak red shifts. When TiO_2 shell is added to the gold nanoparticle core, the absorption peak shifts to the longer wavelength. When less than 10 nm, the thickness of TiO_2 shell has little effect on the absorption spectrum. The simulated results match the experimental measurements.

The objectives of this Master thesis are: 1) to learn basic organic/inorganic chemistry knowledge, 2) to develop basic experimental skills, 3) to be familiar with useful characterization tools, 4) to demonstrate the feasibility of template method in making nanoparticles, 5) to grasp the simulation techniques, and 6) to improve both experimental and analytical abilities.

4.2 Future Work

Other types of nanoparticles can be crafted by using different polymer templates. According to Pang et al [2], P4VP-*b*-PtBA-*b*-PS can be used to produce core-shell nanoparticles. It is also possible to synthesize nanoparticles with more complicated morphology by modifying the polymer templates.

By using the template method, nanoparticle made of desired materials can be yielded. In light of applications, for example, Fe_3O_4/Au core shell nanoparticles can by synthesized to satisfy the need of biological targeting, medical imaging, cancer therapy, etc, and $BaTiO_3$ nanoparticles can be used in ferroelectric-related applications.

Simulation can also be carried out in conjunction with the nanoparticle preparation to guide, optimize, and confirm the experimental results.

APPENDIX

COMSOL SIMULATION SETUP

Example: Au(15nm)/TiO_2(5nm)

Report generated by COMSOL.

1 Global

Global settings

Name	Gold_TiO2.mph
Path	D:\comsol\ Gold_TiO2.mph
Program	COMSOL 4.4
Unit system	SI

Used products

COMSOL Multiphysics
RF Module

1.1 Definitions

1.1.1 Parameters 1

Parameters

Name	Expression	Value	Description
wl	500[nm]	5.0000E-7 m	
k	2*pi/wl	1.2566E7 1/m	
f	c_const/wl	5.9958E14 1/s	
r	15[nm]	1.5000E-8 m	
rs	5[nm]	5.0000E-9 m	
r_water	wl/2	2.5000E-7 m	
r_pml	wl/4	1.2500E-7 m	
waterRe	1.7822	1.7822	
waterIm	2.67e-9	2.67E-9	
watersigma	2*pi*f*waterIm*(8.854e-12 [F/m])	8.9060E-5 S/m	

1.1.2 Functions

Interpolation 1

Function name	goldRe
Function type	Interpolation

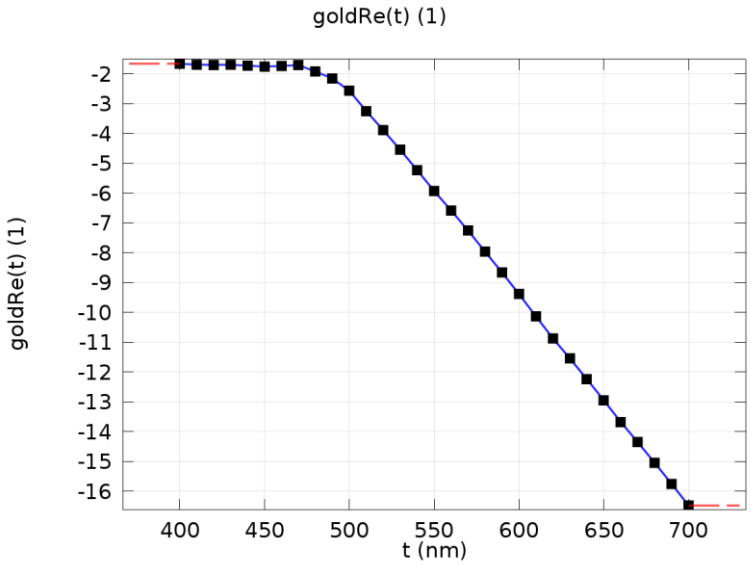

Interpolation 1

Interpolation 2

Function name	goldIm
Function type	Interpolation

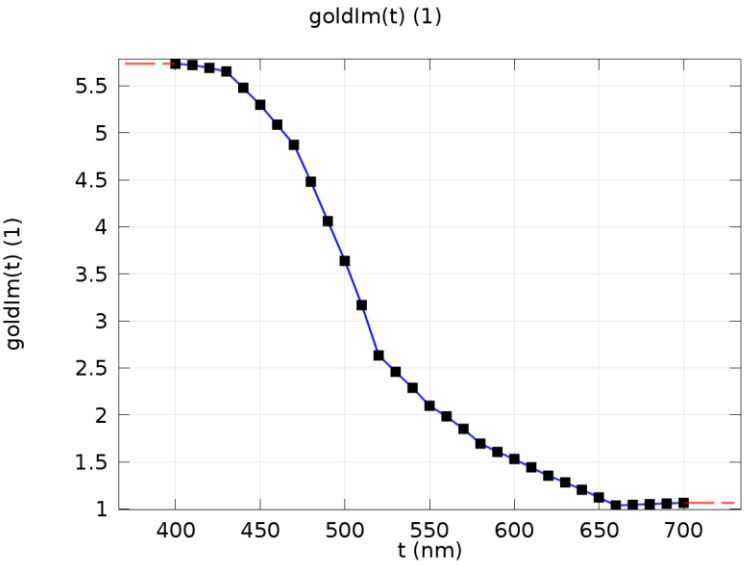

Interpolation 2

Interpolation 3

Function name	TiO2Re
Function type	Interpolation

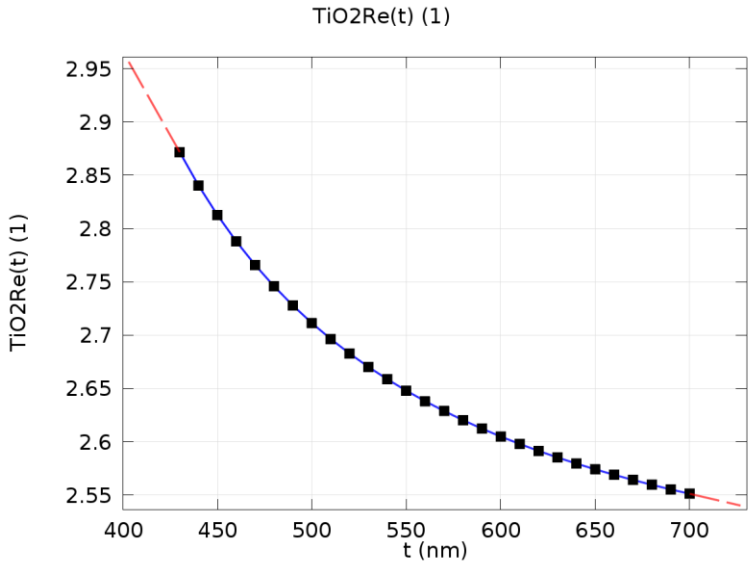

Interpolation 3

2 Component

Component settings

Unit system	SI
Geometry shape order	automatic

2.1 Definitions

2.1.1 Coordinate Systems

Boundary System 1

Coordinate system type	Boundary system
Tag	sys1

Settings

First (t1)	Second (n)	Third (to)
t1	n	to

Settings

Name	Value
Create first tangent direction from	Global Cartesian

2.1.2 Domain Properties

Perfectly Matched Layer 1

Tag	pml1

Selection

Geometric entity level	Domain
Selection	Domains 1–2, 5, 8

Geometry

Name	Value
Coordinate names	{x, y, z}
Type	Cylindrical

Settings

Name	Value
Center coordinate	{0, 0}
Typical wavelength from	Physics interface
Physics	Electromagnetic Waves, Frequency Domain

Scaling

Name	Value
Coordinate stretching type	Polynomial

2.2 Geometry

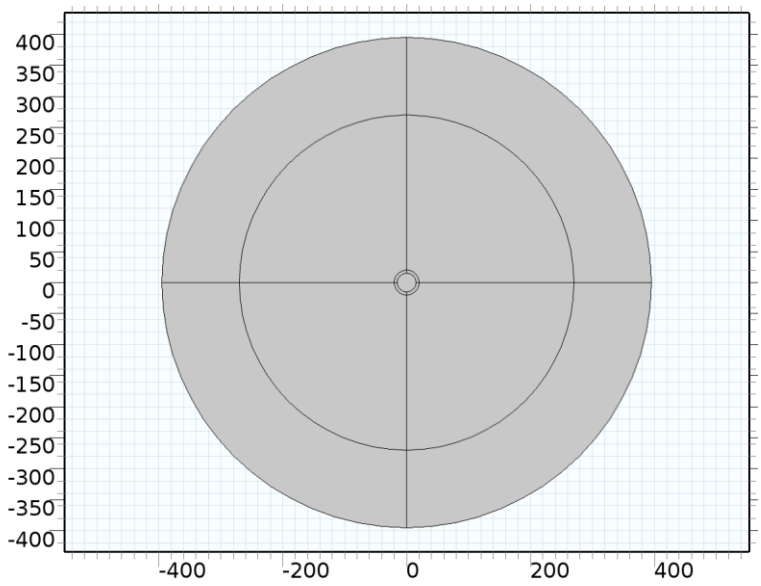

Geometry 1

Units

Length unit	nm
Angular unit	deg

2.2.1 Circle 1 (c1)

Position

Name	Value
Position	{0, 0}

Position

Layer name	Thickness (nm)
Layer 1	r_pml
Layer 2	r_water
Layer 3	rs

Size and shape

Name	Value
Radius	r + rs + r_water + r_pml

2.3 Materials

2.3.1 water

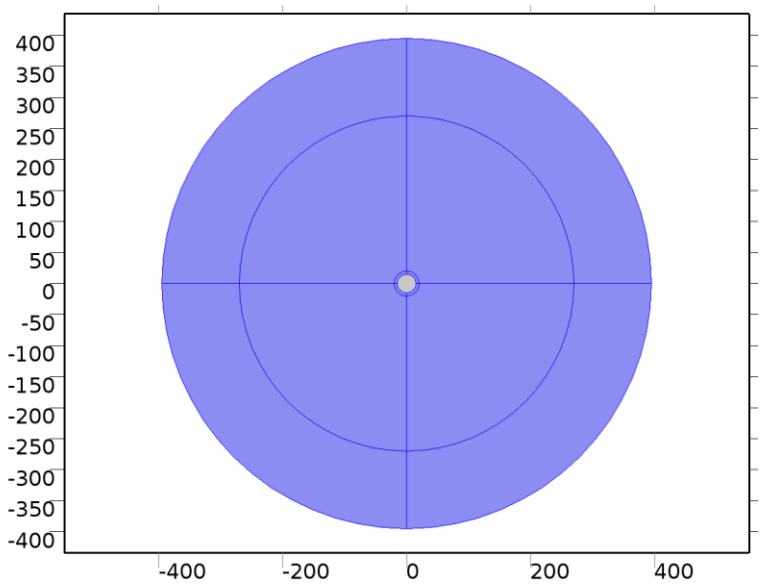

water

Selection

Geometric entity level	Domain
Selection	Domains 1–12

Material parameters

Name	Value	Unit
Relative permeability	1	1
Electrical conductivity	2*pi*f*waterIm*(8.854e-12[F/m])	S/m
Relative permittivity (imaginary part)	waterIm	1
Relative permittivity (real part)	waterRe	1

2.3.2 gold core

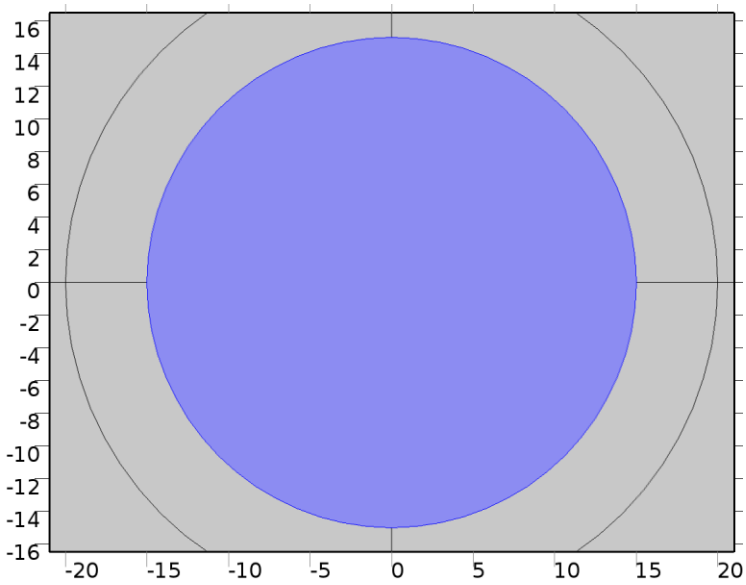

gold core

Selection

Geometric entity level	Domain
Selection	Domain 13

Material parameters

Name	Value	Unit
Relative permeability	1	1
Electrical conductivity	2*pi*f*goldIm(wl)*(8.854e-12[F/m])	S/m
Relative permittivity (imaginary part)	goldIm(wl)	1
Relative permittivity (real part)	goldRe(wl)	1

2.4 Electromagnetic Waves, Frequency Domain

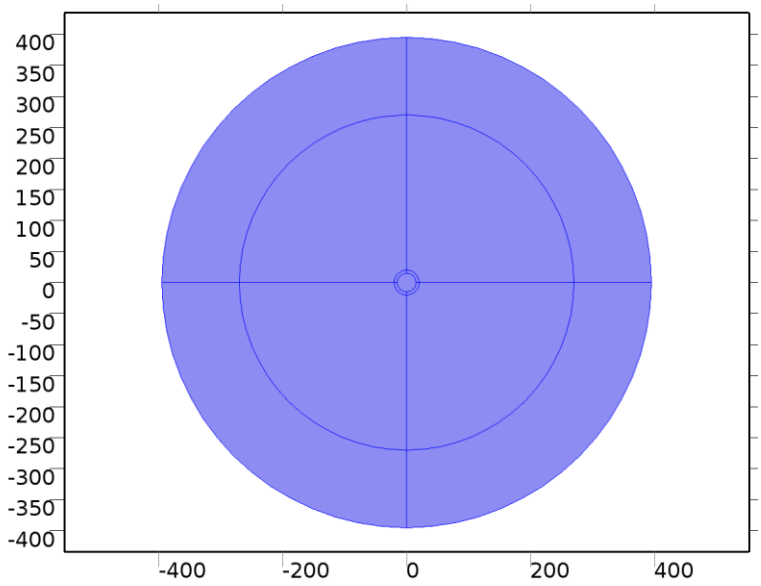

Electromagnetic Waves, Frequency Domain

Selection

Geometric entity level	Domain
Selection	Domains 1–13

Equations

$$\nabla \times \mu_r^{-1}(\nabla \times \mathbf{E}) - k_0^2(\varepsilon_r - \frac{j\sigma}{\omega\varepsilon_0})\mathbf{E} = \mathbf{0}$$

$$\mathbf{E}(x,y,z) = \tilde{\mathbf{E}}(x,y)e^{-ik_z z}$$

Settings

Description	Value
Electric field	Quadratic
Value type when using splitting of complex variables	Complex
Electric field components solved for	In - plane vector
Solve for	Scattered field
Background wave type	User defined
Background electric field, x component	0
Background electric field, y component	exp(-j*k*x)
Background electric field, z component	0
Activate port sweep	Off
Enable	Off
Methodology options	Robust

Used products

COMSOL Multiphysics
RF Module

2.4.1 Wave Equation, Electric 1

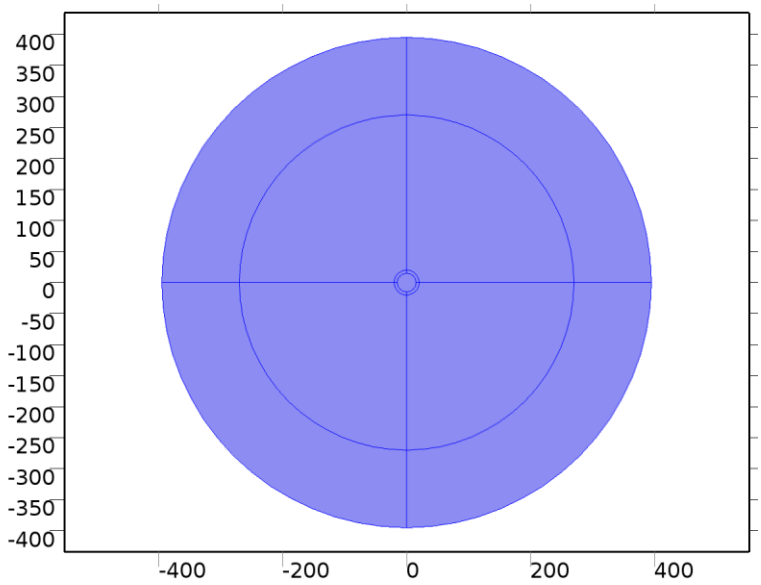

Wave Equation, Electric 1

Selection

Geometric entity level	Domain
Selection	Domains 1–13

Equations

$$\nabla \times \mu_r^{-1}(\nabla \times \mathbf{E}) - k_0^2(\epsilon_r - \frac{j\sigma}{\omega\epsilon_0})\mathbf{E} = \mathbf{0}$$

$$\mathbf{E}(x,y,z) = \tilde{\mathbf{E}}(x,y)e^{-ik_z z}$$

Settings

Description	Value
Electric displacement field model	Dielectric loss
Relative permittivity (imaginary part)	From material
Relative permittivity (imaginary part)	{{0, 0, 0}, {0, 0, 0}, {0, 0, 0}}
Relative permittivity (real part)	From material
Relative permittivity (real part)	{{1, 0, 0}, {0, 1, 0}, {0, 0, 1}}
Refractive index	{{1, 0, 0}, {0, 1, 0}, {0, 0, 1}}
Refractive index, imaginary part	{{0, 0, 0}, {0, 0, 0}, {0, 0, 0}}
Relative permittivity	{{1, 0, 0}, {0, 1, 0}, {0, 0, 1}}
Relative permittivity, high-frequency	{{1, 0, 0}, {0, 1, 0}, {0, 0, 1}}
Constitutive relation	Relative permeability
Relative permeability	From material
Relative permeability	{{1, 0, 0}, {0, 1, 0}, {0, 0, 1}}
Electrical conductivity	From material
Electrical conductivity	{{0, 0, 0}, {0, 0, 0}, {0, 0, 0}}

Properties from material

Property	Material	Property group
Relative permittivity (imaginary part)	water	Dielectric losses
Relative permittivity (real part)	water	Dielectric losses
Relative permeability	water	Basic
Electrical conductivity	water	Basic
Relative permittivity (imaginary part)	gold core	Dielectric losses
Relative permittivity (real part)	gold core	Dielectric losses
Relative permeability	gold core	Basic
Electrical conductivity	gold core	Basic

2.4.2 Perfect Electric Conductor 1

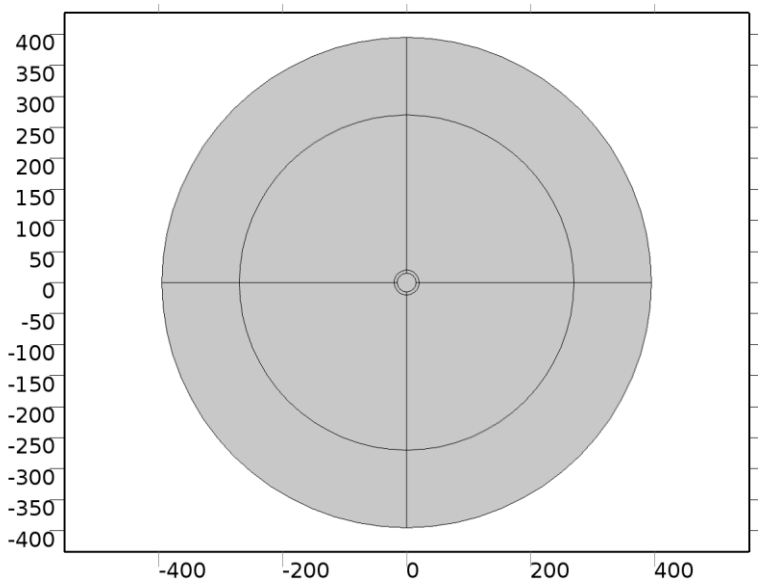

Perfect Electric Conductor 1

Selection

Geometric entity level	Boundary
Selection	No boundaries

Equations

$$\mathbf{n} \times \mathbf{E} = 0$$

Settings

Description	Value
Apply reaction terms on	All physics (symmetric)
Use weak constraints	Off
Constraint method	Elemental

2.4.3 Initial Values 1

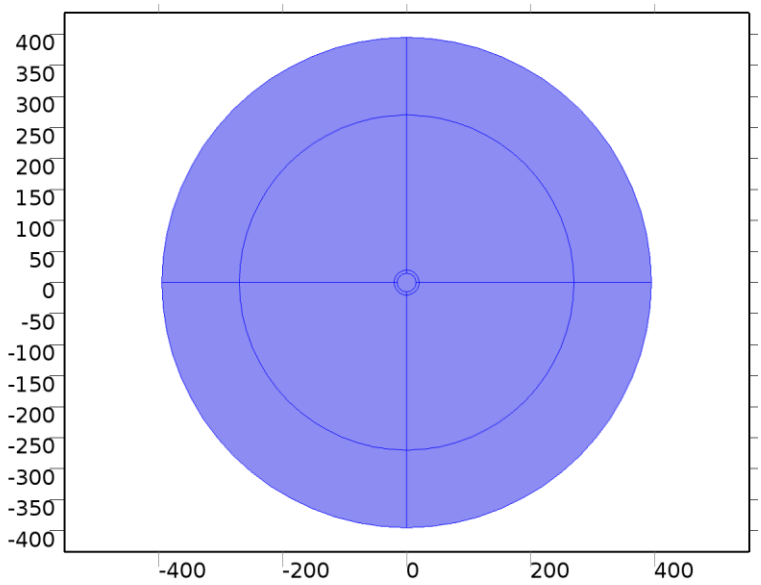

Initial Values 1

Selection

Geometric entity level	Domain
Selection	Domains 1–13

Settings

Description	Value
Electric field	{0, 0, 0}

2.4.4 Scattering Boundary Condition 1

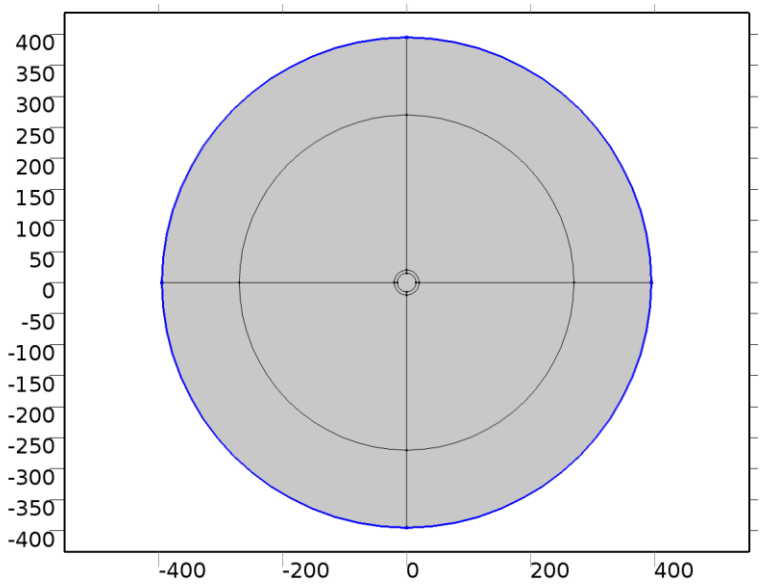

Scattering Boundary Condition 1

Selection

Geometric entity level	Boundary
Selection	Boundaries 13–14, 21, 28

Equations

$$\mathbf{n} \times (\nabla \times (\mathbf{E} + \mathbf{E}_b)) - jk\mathbf{n} \times (\mathbf{E} \times \mathbf{n}) = 0$$

Settings

Description	Value
Incident electric field, x component	0
Incident electric field, y component	0
Incident electric field, z component	exp(-j*k*x)
Scattered wave type	Plane wave
Incident wave direction, x component	-emw.nx
Incident wave direction, y component	-emw.ny
Incident wave direction, z component	0
Order	First order

2.5 Mesh

Mesh statistics

Property	Value
Minimum element quality	0.0
Average element quality	0.0

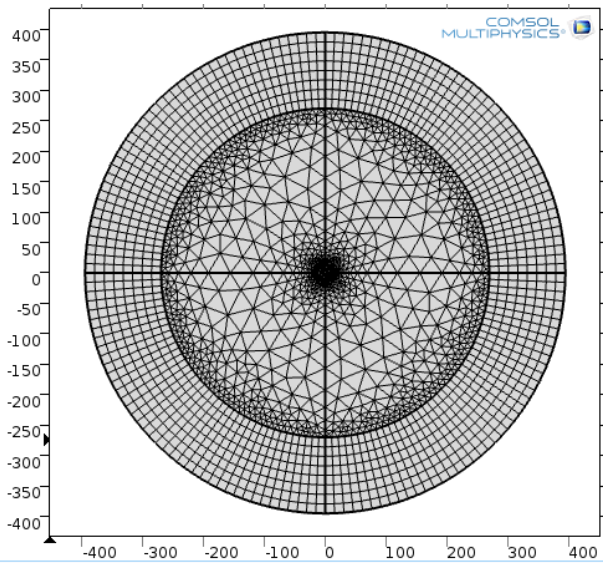

Mesh 1

2.5.1 Size (size)

Settings

Name	Value
Maximum element size	52.9
Minimum element size	0.237

Name	Value
Curvature factor	0.3
Maximum element growth rate	1.3

2.5.2 Mapped 1 (map1)

Selection

Geometric entity level	Domain
Selection	Domains 1–2, 7, 12

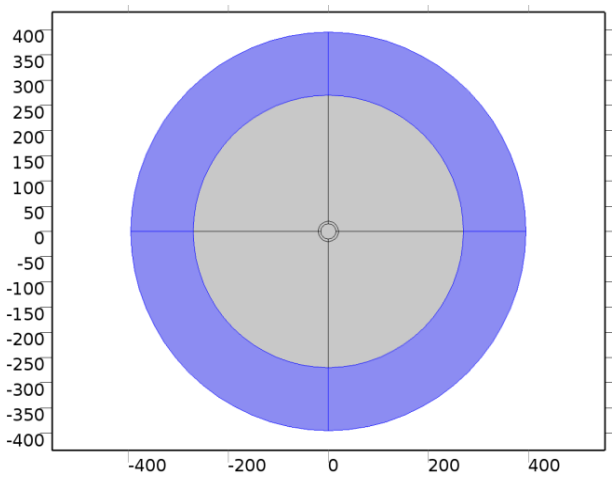

Mapped 1

Size 1 (size1)

Selection

Geometric entity level	Domain
Selection	Domains 1–2, 7, 12

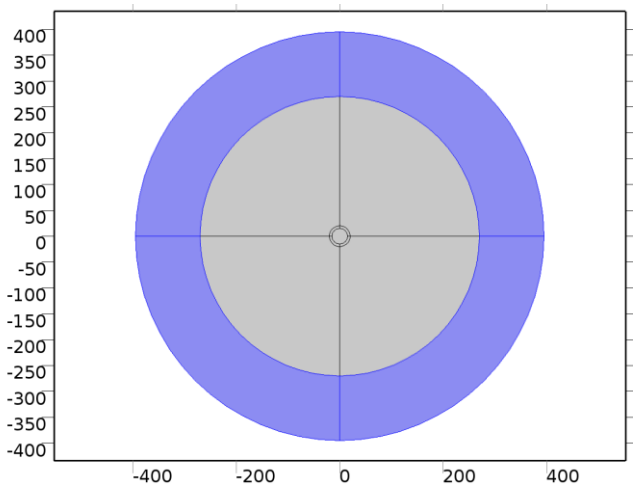

Size 1

Settings

Name	Value
Maximum element size	15.8
Minimum element size	0.0593
Curvature factor	0.25
Maximum element growth rate	1.2
Predefined size	Extra fine

2.5.3 Free Triangular 1 (ftri1)

Selection

Geometric entity level	Remaining

3 Study

3.1 Parametric Sweep

Parameter name	Parameter value list
wl	range(400[nm],1[nm],700[nm])

3.2 Frequency Domain

Study settings

Property	Value
Include geometric nonlinearity	Off

Frequencies: f

Physics and variables selection

Physics interface	Discretization
Electromagnetic Waves, Frequency Domain (emw)	physics

Mesh selection

Geometry	Mesh
Geometry 1 (geom1)	mesh1

REFERENCES

[1] S. Eustis and M.A. El-Sayed, "Why gold nanoparticles are more precious than pretty gold: Noble metal surface Plasmon resonance and its enhancement of the radiative and nonradiative properties of nanocrystals of different shapes," *Chemical Society Reviews*, vol. 35, pp. 207, 2006.

[2] X. Pang, et al, "A general and robust strategy for the synthesis of nearly monodisperse colloidal nanocrystals," *Nature Nanotechnology*, vol. 8, pp. 426, 2013.

[3] T. E. Patten and K, Matyjaszewski, "Atom transfer radical polymerization and the synthesis of polymeric materials," *Advanced Materials*, vol. 10, pp. 901, 1998.

[4] G. Odian, "Principles of polymerization," in Radical Chain Polymerization. New York: Wiley-Interscience, 2004, pp. 316.

[5] K. Matyjaszewski and J. Xia, "Atom transfer radical polymerization," *Chemical Reviews*, vol. 101, no. 9, pp. 2921, 2001.

[6] M. Sartor, Dynamic light scattering. [Online] Available: https://physics.ucsd.edu/neurophysics/courses/physics_173_273/dynamic_light_scattering_03.pdf

[7] P. K. Jain and M. A. El-Sayed, "Universal scaling of Plasmon coupling in metal nanostructures: extension from particle pairs to nanoshells," *Nano Letters*, vol. 7, no. 9, pp. 2854, 2007.

[8] U. Kreibig and M. Vollmer, "Optical properties of metal clusters." New York: Springer, 1995.

[9] J. L. Hammond, "Localized surface plasmon resonance as a biosensing platform for developing countries," *Biosensor*, vol. 4, no. 2, pp. 172, 2014.

[10] S.Yushanov, J. S. Crompton, and K. C. Koppenhoefer, "Mie scattering of electromagnetic waves," AltaSim Technologies.

[11] X. Pang, et al, "Novel amphiphilic multi-arm, star-like block copolymers as unimolecular micelles," *Macromolecules*, vol. 44, pp. 3746, 2011.

[12] J. Yuan, et al, "Water-soluble organo-silica hybrid nanowires," *Nature Materials*, vol. 7, pp. 718, 2008.

[13] J. K. Lee, et al, "Silicon nanoparticles-graphene paper composites for lithium ion battery anodes," *Chemical Communications*, vol. 46, no. 12, pp. 2025, 2010.

[14] M. Stupca, et al, "Enhancement of polycrystalline silicon solar cells using ultrathin films of silicon nanoparticles," *Applied Physics Letters*, vol. 91, no. 6, 2007.

[15] P. B. Johnson and R.W. Christy, "Optical constants of the noble metals," *Physical Review B*, vol. 6, no. 12, pp. 4370, 1972.

[16] J. R. Devore, "Refractive indices of Rutile and Sphalerite," *Journal of the Optical Society of America*, vol. 41, issue. 6, pp. 416, 1951.

[17] W. Knoll, "Interfaces and thin films as seen by bound electromagnetic waves," *Annual Review of Physical Chemistry*, vol. 49, pp. 569, 1998.

[18] Gold nanoparticles: optical properties. [Online] Available: http://nanocomposix.com/pages/gold-nanoparticles-optical-properties

[19] X. Zhang, et al, "Plasmonic photocatalysis," *Reports on Progress in Physics*, vol. 76, issue. 4, pp. 046401, 2013.

[20] W. L. Liu, et al, "The influence of shell thickness of Au@TiO_2 core-shell nanoparticles on the plasmonic enhancement effect in dye-sensitized solar cells," *Nanoscale*, vol. 5, pp. 7953, 2013.